

Advances in Optical Technologies

Nanophotonics: Fabrications and Application of Nanoscale Optics to Novel Photonic Devices

Guest Editors: Takashi Yatsui, Chennupati Jagadish,
and Gilles Lerondel





Nanophotonics: Fabrications and Application of Nanoscale Optics to Novel Photonic Devices

Advances in Optical Technologies

Nanophotonics: Fabrications and Application of Nanoscale Optics to Novel Photonic Devices

Guest Editors: Takashi Yatsui, Chennupati Jagadish,
and Gilles Lerondel



Copyright © 2015 Hindawi Publishing Corporation. All rights reserved.

This is a special issue published in “Advances in Optical Technologies.” All articles are open access articles distributed under the Creative Commons Attribution License, which permits unrestricted use, distribution, and reproduction in any medium, provided the original work is properly cited.

Editorial Board

Mustafa A. G. Abushagur, USA
Partha P. Banerjee, USA
Ralph Barry Johnson, USA
Augusto Beléndez, Spain
Steve Blair, USA
Maria Luisa Calvo, Spain
Zhongping Chen, USA
Fu-Pen Chiang, USA
Petr Eliseev, USA
Michael A. Fiddy, USA
Richard B. Hoover, USA

Zoran Ikonc, UK
Saulius Juodkazis, Australia
Mark A. Kahan, USA
Alexander A. Kaminskii, Russia
Qiang Lin, China
Liren Liu, China
Qingming Luo, China
Daniel Malacara, Mexico
Mikhail Noginov, USA
Markus Pessa, Finland
Giancarlo C. Righini, Italy

José Luís Santos, Portugal
Paramasivam Senthilkumaran, India
Colin J. R. Sheppard, Singapore
Kiyoshi Shimamura, Japan
Jagdish P. Singh, USA
Yinglin Song, China
Theo Tschudi, Germany
Leonid P. Yaroslavsky, Israel
Jianping Yin, China
Yong Zhao, China

Contents

Nanophotonics: Fabrications and Application of Nanoscale Optics to Novel Photonic Devices,
Takashi Yatsui, Chennupati Jagadish, and Gilles Lerondel
Volume 2015, Article ID 609682, 1 page

Switching the Localized Surface Plasmon Resonance of Single Gold Nanorods with a Phase-Change Material and the Implementation of a Cellular Automata Algorithm Using a Plasmon Particle Array,
Takashi Hira, Takayuki Uchiyama, Kenta Kuwamura, Yuya Kihara, Tasuku Yawatari, and Toshiharu Saiki
Volume 2015, Article ID 150791, 5 pages

GaP Homojunction LEDs Fabricated by Dressed-Photon-Phonon-Assisted Annealing, Jun Hyoung Kim,
Tadashi Kawazoe, and Motoichi Ohtsu
Volume 2015, Article ID 236014, 8 pages

Realization of Ultraflat Plastic Film Using Dressed-Photon-Phonon-Assisted Selective Etching of Nanoscale Structures, Takashi Yatsui, Wataru Nomura, and Motoichi Ohtsu
Volume 2015, Article ID 701802, 5 pages

Emission Spectral Control of a Silicon Light Emitting Diode Fabricated by Dressed-Photon-Phonon Assisted Annealing Using a Short Pulse Pair, Tadashi Kawazoe, Naoki Wada, and Motoichi Ohtsu
Volume 2014, Article ID 958327, 8 pages

Demonstration of Controlling the Spatiotemporal Dynamics of Optical Near-Field Excitation Transfer in Y-Junction Structure Consisting of Randomly Distributed Quantum Dots, Wataru Nomura,
Makoto Naruse, Masashi Aono, Song-Ju Kim, Tadashi Kawazoe, Takashi Yatsui, and Motoichi Ohtsu
Volume 2014, Article ID 569684, 8 pages

Editorial

Nanophotonics: Fabrications and Application of Nanoscale Optics to Novel Photonic Devices

Takashi Yatsui,¹ Chennupati Jagadish,² and Gilles Lerondel³

¹*School of Engineering, University of Tokyo, Bunkyo-ku, Tokyo 113-8656, Japan*

²*Department of Electronic Materials Engineering, Research School of Physics and Engineering, Australian National University, Canberra, ACT 0200, Australia*

³*Laboratoire de Nanotechnologie et d'Instrumentation Optique, Institut Charles Delaunay, CNRS UMR 6281, Université de Technologie de Troyes, CS 42060, 10004 Troyes Cedex, France*

Correspondence should be addressed to Takashi Yatsui; yatsui@ee.t.u-tokyo.ac.jp

Received 27 November 2014; Accepted 27 November 2014

Copyright © 2015 Takashi Yatsui et al. This is an open access article distributed under the Creative Commons Attribution License, which permits unrestricted use, distribution, and reproduction in any medium, provided the original work is properly cited.

Nanophotonics is a generic technology that can overcome the deadlock of conventional photonics, in which the size is limited by diffraction limits of light. Based on interdisciplinary studies including condensed-matter physics, optical science, and quantum field theory, nanoscale materials and optical energy transfer at nanoscale have been extensively studied. The recent development on nanoscale optics opens up new concept of nanoscale optical theory, as an example dressed photon theory, and a variety of new phenomena have been investigated. The results of the basic research have been applied to numerous applications, including nanometer-sized photonic devices, nanoscale fabrication techniques, and highly efficient energy conversion. Here, we have invited a few papers that address the above topics.

One paper of this special issue addresses solution searching devices based on the optical near-field energy transfer between quantum dots (QDs). The results shown here indicated the possibility of controlling the spatiotemporal dynamics between multiple QDs, resulting in a higher performance of solution searching devices. Another paper reported the new type of light emitting device (LED) of silicon (Si). Even though Si is an indirect band gap material, they realized Si based LED by introducing dressed photon and phonon (DPP) assisted annealing process. Moreover, the emitting spectrum was controlled by DPP assisted annealing using a short pulse pair. One of the papers also addressed LED but based on GaP, which is also an indirect band gap semiconductor. In this paper, GaP based LED fabricated

by DPP assisted annealing process is reported. Such device has unique emitting properties depending on the annealing process. Another paper demonstrated the possibility of high-contrast switching of local surface plasmon using hybrid structure made of metallic nanorods and a phase change material. Additionally, the authors suggested the one-dimensional cellular automata algorithm using metallic nanorod and phase change material. Another paper reported the unique flattening technique made possible thanks to DPP. By using DPP etching, selective flattening of the smallest surface features is made possible, resulting in an angstrom scale ultraflat plastic substrate.

*Takashi Yatsui
Chennupati Jagadish
Gilles Lerondel*

Research Article

Switching the Localized Surface Plasmon Resonance of Single Gold Nanorods with a Phase-Change Material and the Implementation of a Cellular Automata Algorithm Using a Plasmon Particle Array

Takashi Hira, Takayuki Uchiyama, Kenta Kuwamura, Yuya Kihara, Tasuku Yawatari, and Toshiharu Saiki

Department of Electronics and Electrical Engineering, Keio University, 3-14-1 Hiyoshi, Kohoku, Yokohama 223-8522, Japan

Correspondence should be addressed to Toshiharu Saiki; saiki@elec.keio.ac.jp

Received 20 August 2014; Revised 9 October 2014; Accepted 9 October 2014

Academic Editor: Takashi Yatsui

Copyright © 2015 Takashi Hira et al. This is an open access article distributed under the Creative Commons Attribution License, which permits unrestricted use, distribution, and reproduction in any medium, provided the original work is properly cited.

We investigate the modulation of the localized surface plasmon resonance (LSPR) of a gold nanorod (AuNR) using a GeSbTe film as an active medium. We demonstrate high-contrast switching of LSPR in an AuNR/GST/Au thin film sandwich structure upon phase change. To go beyond this single-particle switching functionality, we consider a plasmon particle system interacting with a phase-change material (PCM) to discuss the possibility of parallel processing devices with memory functionality, exploiting the plasticity and threshold behavior that are inherent characteristics of PCMs. We demonstrate that the temporal and spatial evolution of a plasmon-PCM array system can be equivalent to a cellular automata algorithm.

1. Introduction

Control of localized surface plasmon resonance (LSPR) excited on metal nanostructures has drawn attention for applications in dynamic switching and for tuning the functionality of plasmonic optical devices [1, 2]. Basically, control of LSPR relies on its sensitivity to the optical permittivity of the environment due to dielectric screening and mode hybridization [3, 4]. As reversible active media for LSPR control, chalcogenide phase-change materials (PCMs) [5] such as GeSbTe are promising for the development of high-contrast robust plasmonic switching devices [6–8] owing to significant differences in the dielectric constants of their crystalline and amorphous phases, as well as their stable plasticity at room temperature and their rapid crystallization (within several tens of nanoseconds). More importantly, GeSbTe can be nonthermally amorphized on a subpicosecond timescale with femtosecond laser pulse excitation [9, 10]. By exploiting these attractive properties of GeSbTe, we have demonstrated the LSPR switching of individual Au nanospheres on a GeSbTe thin film by alternating irradiation by a femtosecond pulse

laser for amorphization and a continuous wave (cw) laser for crystallization [11].

The metal-dielectric-metal nanosandwich structure is an effective approach for enhancing LSPR switching contrast. When two metal particles are coupled, their dipoles are hybridized and split into symmetric and antisymmetric modes. The latter mode is called a magnetic dipole mode, in which the dipole moments of the two particles are aligned in opposite directions and generate a current loop [12–15]. The LSPR peak positions of the hybridized modes, particularly the magnetic dipole mode, shift dramatically with the refractive index of the dielectric material owing to the retardation effect.

Owing to the plasticity and the threshold behavior during both amorphization and crystallization of PCMs, PCM-based LSPR switching elements possess a dual functionality of memory and processing. Integration of LSPR switching elements so that they interact with each other will allow us to build a new computing device. In this paper, as a specific demonstration of this idea, we discuss the implementation of a cellular automata (CA) algorithm [16, 17] into interacting LSPR switching elements. CA is used as a tool for

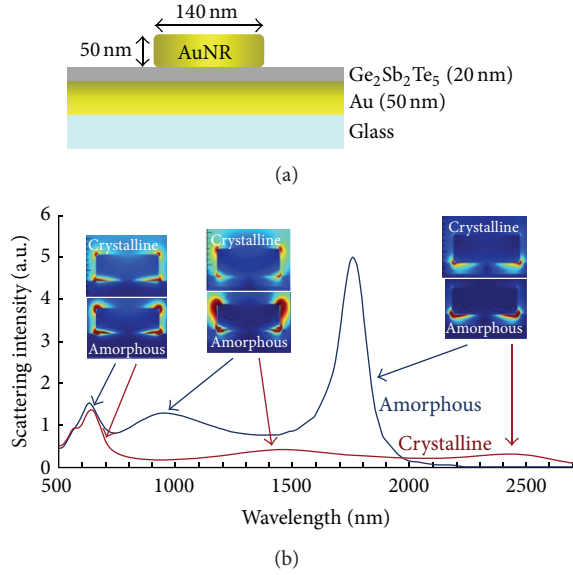


FIGURE 1: (a) Model of the AuNR/GST/Au nanosandwich structure for numerical calculation. (b) Numerically calculated scattering spectra from an AuNR/GST/Au nanosandwich for crystalline and amorphous GST. The insets show the electric field distributions in the vicinity of the AuNR for the three dominant bands.

the modeling of complex and dynamic systems, including natural and social phenomena. Any CA system is composed of cells with a finite number of states, and each cell interacts with neighboring cells. The interaction is local, with the next state of a cell being a function of the current state of itself and its neighbors. In the model we propose that PCM cells, which can be in one of two states (amorphous and crystalline), are allowed to interact with each other by being linked by a gold nanorod (AuNR), whose LSPR peak wavelength is determined by the phase of PCM cells on either side. The CA program proceeds by irradiating with a light pulse train. The local rule set is defined by the temperature rise in the PCM cells induced by the LSPR of the Au nanorod, which is subject to the intensity and wavelength of the irradiating pulse.

2. FDTD Simulation

Figure 1(a) illustrates the layered configuration of the Au and $\text{Ge}_2\text{Sb}_2\text{Te}_5$ (GST) sandwich structure. Numerical simulations based on the finite-difference time-domain (FDTD) method were conducted to determine the appropriate wavelength at which to monitor the LSPR switching of the AuNR. A scattering spectrum of the AuNR was calculated under broadband plane wave illumination at normal incidence. The spatial discretization was set to 1 nm, and the dielectric constants of Au and GST were obtained from [18, 19], respectively. Figure 1(b) shows scattering spectra from the AuNR with crystalline and amorphous phases of the GST layer. The spectrum consists of three dominant bands around 600, 1000, and 1800 nm for amorphous GST and 600, 1500, and 2500 nm for crystalline GST.

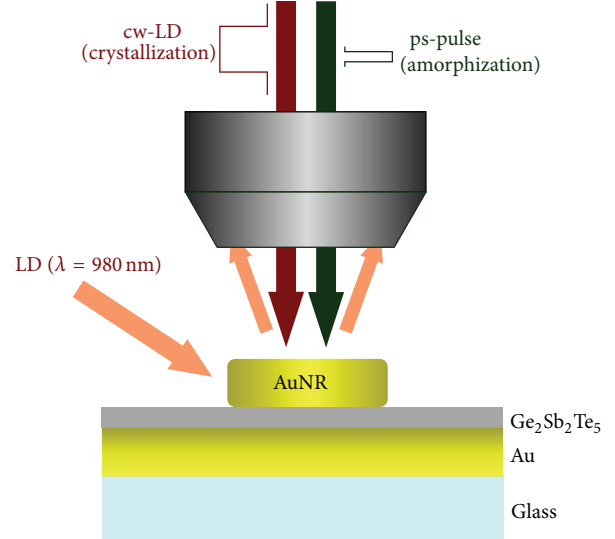


FIGURE 2: Experimental setup for dark-field scattering measurement of single Au nanorods.

The electric field distribution (Figure 1(b) inset) confirms that the lowest bands come from interactions between the AuNR and the underlying Au layer. As in the nanosandwich, this band originates from antisymmetric coupling between the AuNR dipole and its image in the Au layer. The magnetic field intensity distribution (not shown) provides support for this peak assignment; the antisymmetric mode generates a magnetic moment due to the induced electrical dipoles, which oscillate out-of-phase to create an effective current loop.

The LSPR peak position and broadening were significantly altered upon phase change ($\Delta\lambda \approx 500$ nm for the intermediate band and $\Delta\lambda \approx 700$ nm for the lowest band). The higher refractive index of the crystalline phase than that of the amorphous phase causes a larger retardation effect, and thus the LSPR occurs at a longer wavelength. The broader LSPR for crystalline GST is due to the larger imaginary component of the GST dielectric constant, which causes a stronger damping of the LSPR. A high switching contrast is expected around 1000 and 1800 nm, so the former band was selected to demonstrate this, and the scattering intensity ratio of the AuNR for GST in the amorphous phase to that of GST in the crystalline phase is larger than 5.

3. LSPR Switching of a Single Gold Nanorod

After the deposition of a 50-nm-thick Au thin film on a glass substrate, a 20-nm-thick GST film was formed by sputtering. A colloidal solution of AuNRs (140 nm long, 50 nm in diameter) was used, and an AuNR dispersion in ethanol was drop-cast onto the GST film. The substrate was heated to rapidly evaporate the ethanol and prevent the aggregation of AuNRs.

The optical setup for single-AuNR spectroscopy is illustrated in Figure 2. To amorphize the GST, a picosecond pulse from a diode-pumped solid-state laser ($\lambda = 532$ nm; pulse

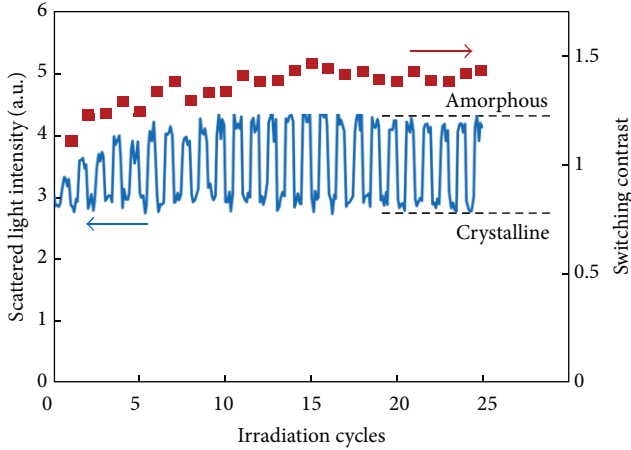


FIGURE 3: Time trace of scattered light intensity ($\lambda = 980$ nm) from AuNR/GST/Au nanosandwich demonstrating repeatable modulation of LSPR band by alternate irradiation with femtosecond pulsed laser for amorphization and cw LD for crystallization. The switching contrast for each cycle is also plotted.

width: 300 ps) was delivered through a microscope objective. The pulse fluence was approximately 200 mJ/cm^2 . To induce crystallization, a laser diode (LD) with $\lambda = 830$ nm was used under cw operation. To monitor the switching behavior of a single AuNR at an LSPR band around 1000 nm, the AuNR was illuminated by a LD with $\lambda = 980$ nm in dark-field configuration, and the scattered light was detected through the objective.

Figure 3 shows a time trace of the scattered light intensity. Starting with the GST layer in the crystalline phase, amorphization and crystallization were repeated under alternating irradiation by picosecond laser pulses and the cw LD. LSPR switching with good stability and repeatability was observed. Here, we define the switching contrast, I_a/I_c , where I_a and I_c are the scattered light intensities for substrates in the amorphous and crystalline phases, respectively. The obtained switching contrast of 1.5 was smaller than expected on the basis of the numerical simulations. This may be due to residual background scattered light originating from the roughness of the GST film surface. The amorphization process may be localized, occurring only in a small volume just below the AuNR, where the electric field enhancement occurs. However, we assumed in the simulation that the GST was fully amorphized throughout the entire volume. This could also explain the deviation from the simulation results.

In the initial stage of the switching operation, a gradual increase in the modulation contrast was observed. Although it was difficult to determine what was occurring from the optical measurements alone, one possible explanation is as follows. The modification of the surface morphology due to volume expansion of the GST film may be different after each amorphization process. There is a volume expansion of approximately 10% upon amorphization from crystalline GST [20]. Therefore, there could be a slight change in the position or configuration of the AuNR in the initial stage that eventually becomes stabilized.

4. Implementation of Cellular Automata Algorithm

We attempted to implement a CA [16, 17] algorithm into the interacting LSPR switching elements. A CA consists of a uniform array of identical cells in which each cell has a finite number of states and interacts with a few neighboring cells. A rule set is provided to define how each cell is updated at each new time step as a result of its interactions. The rule set may involve some physical mechanism that takes account of local interactions.

One very simple CA is a one-dimensional line of cells, each existing in one of two states (0 or 1). The local transition rule for each cell is defined as a function of the adjacent two neighbors. Figure 4 illustrates a one-dimensional CA composed of plasmon particles and a phase change material. GeSbTe nanopads are arranged in a regular array on an Au film. Each nanopad corresponds to a cell in the CA. Some pads are in the crystalline phase (state “0”), while others are in the amorphous phase (state “1”). In order to enable interaction between neighboring nanopads, they are coupled to each other by AuNRs. When the system is uniformly illuminated with laser light at a specific wavelength, some nanorods resonate with the light while others do not, depending on whether the nanopads on both sides are amorphous or crystalline. If a nanorod resonates with the light, the nanopads on both sides absorb more light and are heated, and eventually a phase change may take place depending on what temperature the nanopad reaches.

An electromagnetic simulation was performed to calculate the temperature increase in the nanopads under light irradiation at different wavelengths. The model unit element of the CA used for this calculation is illustrated in Figure 5(a). After solving for the electric field distribution using the FDTD method, we calculated the absorbed power density (Q_{abs}) distribution within the nanopad, employing the imaginary part of the permittivity of crystalline and amorphous GST. Figure 5(b) shows the temperature of nanopads in different configurations as a function of irradiation wavelength. Here, we assume that the temperature increase in a nanopad due to light absorption is proportional to the heat generated, which can be obtained by integrating Q_{abs} over the volume of the nanopad. The irradiation light intensity was determined such that the maximum temperature of a nanopad in the crystalline phase exceeded the melting point of GST ($\sim 600^\circ\text{C}$). For example, if the wavelength is 1800 nm and the two nanopads adjacent to an Au nanorod are in the amorphous phase, the temperature will reach 350°C . Furthermore, if one pad is amorphous and the other is crystalline, the temperature of the crystalline nanopad will increase to 950°C , while the other only reaches 70°C .

In a one-dimensional CA (array of nanopads), the temperature of each nanopad can be calculated in a similar fashion. The laser irradiation conditions are generally different for amorphization and crystallization. However, although somewhat hypothetical, if we assume an irradiation light pulse with a width longer than the crystallization time and with a fall time much shorter than the crystallization time, the pulse can induce both amorphization and crystallization,

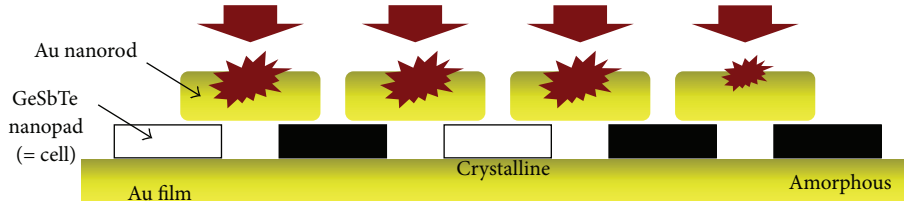


FIGURE 4: One-dimensional CA model of GeSbTe nanopads. The nanopads are coupled to each other by Au nanorods.

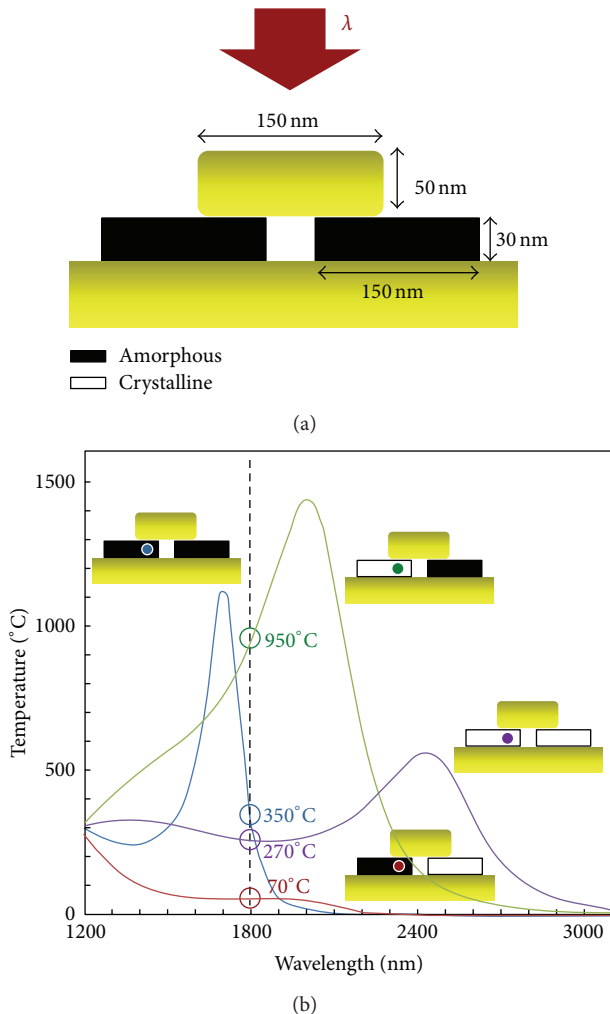


FIGURE 5: (a) Model for electromagnetic and thermal simulations. (b) Maximum temperature of the nanopads as a function of irradiation wavelength.

depending solely on the temperature rise. To determine the states (crystalline or amorphous) for the subsequent time step, we make the following simple assumptions. (1) If the temperature exceeds the melting point of GST, the crystalline phase will become amorphous. (2) Between the crystallization temperature ($\sim 150^\circ\text{C}$) and the melting point, the amorphous phase will become crystalline. (3) Below the crystallization temperature, nothing will happen. Under

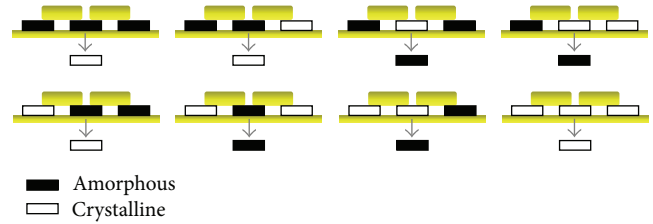


FIGURE 6: Rule number 54 for one-dimensional array of cellular automata.

these assumptions, at an irradiation wavelength of 1800 nm, we obtained the rule set illustrated in Figure 6, called rule number 54. When the irradiation wavelength is shifted, we can obtain another rule set.

5. Conclusion

Single-particle spectroscopy of an Au nanosandwich, in which a thin GST layer is sandwiched between interacting AuNRs and an Au film, was conducted. The LSPR band structure was determined using the FDTD method, and its physical causes were discussed. A very large band shift was obtained for the hybridized modes between the AuNR and Au film upon phase change of the GST layer. An experimental demonstration of LSPR modulation was performed for the LSPR band around 1000 nm, at which a switching contrast of >5 would be expected. Stable and repeatable switching with a contrast of 1.5 was obtained. Finally, as an application of high-contrast LSPR switching, the implementation of a one-dimensional cellular automata algorithm using Au nanorod and GST nanopad array was discussed.

Conflict of Interests

The authors declare that there is no conflict of interests regarding the publication of this paper.

Acknowledgments

The authors are grateful to T. Shintani for providing them with GST thin film samples. This work was supported by JSPS KAKENHI Grant no. 24226006 and partially by Advanced Photon Science Alliance Project from MEXT.

References

- [1] Y. Leroux, J. C. Lacroix, C. Fave et al., "Active plasmonic devices with anisotropic optical response: a step toward active polarizer," *Nano Letters*, vol. 9, no. 5, pp. 2144–2148, 2009.
- [2] N. A. Mirin, K. Bao, and P. Nordlander, "Fano Resonances in plasmonic nanoparticle aggregates," *Journal of Physical Chemistry A*, vol. 113, no. 16, pp. 4028–4034, 2009.
- [3] M. Pelton, J. Aizpurua, and G. Bryant, "Metal-nanoparticle plasmonics," *Laser and Photonics Reviews*, vol. 2, no. 3, pp. 136–159, 2008.
- [4] W. A. Murray and W. L. Barnes, "Plasmonic materials," *Advanced Materials*, vol. 19, no. 22, pp. 3771–3782, 2007.
- [5] M. Wuttig and N. Yamada, "Phase-change materials for rewritable data storage," *Nature Materials*, vol. 6, no. 11, pp. 824–832, 2007.
- [6] Z. L. Sámson, K. F. MacDonald, F. de Angelis et al., "Metamaterial electro-optic switch of nanoscale thickness," *Applied Physics Letters*, vol. 96, no. 14, Article ID 143105, 2010.
- [7] Z. L. Sámson, S.-C. Yen, K. F. MacDonald et al., "Chalcogenide glasses in active plasmonics," *Physica Status Solidi—Rapid Research Letters*, vol. 4, no. 10, pp. 274–276, 2010.
- [8] Y. G. Chen, T. S. Kao, B. Ng et al., "Hybrid phase-change plasmonic crystals for active tuning of lattice resonances," *Optics Express*, vol. 21, no. 11, pp. 13691–13698, 2013.
- [9] M. Konishi, H. Santo, Y. Hongo, K. Tajima, M. Hosoi, and T. Saiki, "Ultrafast amorphization in $\text{Ge}_{10}\text{Sb}_2\text{Te}_{13}$ thin film induced by single femtosecond laser pulse," *Applied Optics*, vol. 49, no. 18, pp. 3470–3473, 2010.
- [10] J. Takeda, W. Oba, Y. Minami, T. Saiki, and I. Katayama, "Ultrafast crystalline-to-amorphous phase transition in $\text{Ge}_2\text{Sb}_2\text{Te}_5$ chalcogenide alloy thin film using single-shot imaging spectroscopy," *Applied Physics Letters*, vol. 104, no. 26, Article ID 261903, 4 pages, 2014.
- [11] T. Hira, T. Homma, T. Uchiyama, K. Kuwamura, and T. Saiki, "Switching of localized surface plasmon resonance of gold nanoparticles on a GeSbTe film mediated by nanoscale phase change and modification of surface morphology," *Applied Physics Letters*, vol. 103, no. 24, Article ID 241101, 2013.
- [12] T. Pakizeh, M. S. Abrishamian, N. Granpayeh, A. Dmitriev, and M. Käll, "Magnetic-field enhancement in gold nanosandwiches," *Optics Express*, vol. 14, no. 18, pp. 8240–8246, 2006.
- [13] A. Dmitriev, T. Pakizeh, M. Käll, and D. S. Sutherland, "Gold-silica-gold nanosandwiches: tunable bimodal plasmonic resonators," *Small*, vol. 3, no. 2, pp. 294–299, 2007.
- [14] Y. Ekinici, A. Christ, M. Agio, O. J. F. Martin, H. H. Solak, and J. F. Löffler, "Electric and magnetic resonances in arrays of coupled gold nanoparticle in-tandem pairs," *Optics Express*, vol. 16, no. 17, pp. 13287–13295, 2008.
- [15] G. Lévêque and O. J. F. Martin, "Optical interactions in a plasmonic particle coupled to a metallic film," *Optics Express*, vol. 14, no. 21, pp. 9971–9981, 2006.
- [16] S. Wolfram, "Statistical mechanics of cellular automata," *Reviews of Modern Physics*, vol. 55, no. 3, pp. 601–644, 1983.
- [17] S. Wolfram, "Cellular automata as models of complexity," *Nature*, vol. 311, no. 5985, pp. 419–424, 1984.
- [18] P. B. Johnson and R. W. Christy, "Optical constants of the noble metals," *Physical Review B*, vol. 6, no. 12, pp. 4370–4379, 1972.
- [19] K. Shportko, S. Kremers, M. Woda, D. Lencer, J. Robertson, and M. Wuttig, "Resonant bonding in crystalline phase-change materials," *Nature Materials*, vol. 7, no. 8, pp. 653–658, 2008.
- [20] V. Weidenhof, I. Friedrich, S. Ziegler, and M. Wuttig, "Atomic force microscopy study of laser induced phase transitions in $\text{Ge}_2\text{Sb}_2\text{Te}_5$," *Journal of Applied Physics*, vol. 86, no. 10, pp. 5879–5887, 1999.

Research Article

GaP Homojunction LEDs Fabricated by Dressed-Photon-Phonon-Assisted Annealing

Jun Hyoung Kim,¹ Tadashi Kawazoe,^{1,2} and Motoichi Ohtsu^{1,2}

¹Department of Electrical Engineering and Information Systems, Graduate School of Engineering, The University of Tokyo, 2-11-16 Yayoi, Bunkyo-ku, Tokyo 113-8656, Japan

²Nanophotonic Research Center, Graduate School of Engineering, The University of Tokyo, 2-11-16 Yayoi, Bunkyo-ku, Tokyo 113-8656, Japan

Correspondence should be addressed to Jun Hyoung Kim; kimjh@nanophotonics.t.u-tokyo.ac.jp

Received 5 August 2014; Revised 6 November 2014; Accepted 10 November 2014

Academic Editor: Gilles Lerondel

Copyright © 2015 Jun Hyoung Kim et al. This is an open access article distributed under the Creative Commons Attribution License, which permits unrestricted use, distribution, and reproduction in any medium, provided the original work is properly cited.

By using a homojunction-structured GaP single crystal, we generated a photon energy higher than the bandgap energy (2.26 eV). The device was fabricated by performing dressed-photon-phonon- (DPP-) assisted annealing, while applying a forward-bias current, on a p-n homojunction structure formed by implanting a dopant (Zn) into an n-type GaP substrate. The DPP-assisted annealing increased the light emission intensity in an energy band above 2.32 eV by at least 550% compared with that before annealing.

1. Introduction

In recent years, there has been interest in light-emitting diodes (LEDs) as high-efficiency light sources, and research and development has been actively carried out, resulting in remarkable technological progress, particularly in the last ten years. High-efficiency semiconductor light-emitting devices based on InGaN (for light emission in the blue-green band) and AlGaInP (for light emission in the green-red band) have been realized and are now in widespread use. However, there are a number of problems that must be solved. One of those is that a metal-organic vapor phase epitaxy (MOVPE) process, which uses toxic gases, is required for growing the substrates. The environmental load is also high since fine particles that are harmful to the human body could be produced [1]. In addition, finding the optimum conditions for the MOVPE process is not simple, and the growth conditions should be strictly controlled [2–5]. Moreover, this approach has a demerit in terms of material resources, including the need for In, which is a rare earth element.

To overcome the problems mentioned above, in this research we focused on GaP as the material and on dressed-photon-phonon- (DPP-) [6, 7] assisted annealing as the

process method. The bandgap energy, E_g , of GaP is 2.26 eV (wavelength, 548 nm). Also, GaP is a low-cost material that can be readily used to grow single crystals with the liquid encapsulated Czochralski (LEC) method, and research into light-emitting devices using GaP has been conducted for a long time, since as early as the 1960s [8, 9]. However, GaP is an indirect transition type semiconductor, and the light-emission efficiency is known to be extremely low since phonon emission and absorption are required for the radiative recombination of electron-hole pairs. A widely known technique for increasing the efficiency is to introduce isoelectronic impurities such as N atoms, and devices based on this approach are commercially available [10]. Isoelectronic impurities capture and localize electrons due to differences in electronegativity with respect to the component atoms of the host crystal. As a result, according to the uncertainty principle, the wave function of the electrons in wavenumber space becomes broader, making radiative recombination possible at yellow and green wavelengths. In addition, GaP LEDs that emit red light by the addition of Zn and O have also been reported [11]. However, the light-emission efficiency is low because of energy loss due to internal relaxation to the isoelectronic impurity levels. Furthermore, only photons

with energies lower than E_g are emitted, since light emission occurs via localized levels in the forbidden band.

On the other hand, if it were possible to effectively utilize the large E_g of GaP, it would be possible to develop a method that overcomes the environment-related problems and technical difficulties mentioned above, as well as to expand the color coverage of GaP LEDs. To this end, in this study we employed a dressed-photon-phonon- (DPP-) assisted annealing method. We have previously used DPPs to develop LEDs based on Si and SiC, which are also indirect transition type semiconductors, like GaP [12–14]. A dressed photon (DP) is a quasiparticle that represents the coupled state of a photon and an electron-hole pair in a nanosize region [7]. Similarly, a DPP is a quasiparticle that represents the coupled state of a DP and multimode coherent phonons in a nanosize region [6, 7]. In other words, by forming an impurity distribution that easily generates an interaction between electron-hole pairs, photons, and phonons inside a crystal, the limitation due to the wavenumber conservation law is relaxed, thus enabling high-efficiency radiative recombination even in an indirect transition type semiconductor [12–14]. The photon energy of this radiative recombination changes by an amount equal to the energies of multimode coherent phonons involved, and therefore, the photon energy of emitted light can be higher than E_g .

In this study, by subjecting a GaP crystal containing a p-n homojunction to DPP-assisted annealing, we obtained strong enhancement of light emission in the 520–540 nm wavelength band.

2. Principles of Light Emission and Processing Using DPPs

In this section, first we explain the principle of light emission using the DPP-assisted process, followed by a discussion of the processing principle. This is because the principle of light emission described below is also used in device processing. The DPP-assisted process [12] brought about as a result of interactions between electron-hole pairs, photons, and phonons in nanosize regions containing impurities is the basic principle of the light emission. During device processing, first, impurities are made to diffuse by changing the energy (via current and photoabsorption) given to the device into heat. In parts that have a nanostructure (impurity distribution) where the DPP-assisted process easily takes place, the energy is converted to light, and therefore, a relative cooling effect occurs [13]. Diffusion of impurities due to heat generation and maintaining the impurity distribution due to the relative cooling are the basic principles of device processing.

The light emission due to the DPP-assisted process can be understood using a model of the DPP levels as shown in Figure 1. Since the wavenumber is supplied from multimode coherent phonons, the DPP dispersion relation is represented by the horizontal green solid line in Figure 1. Since electron-hole pairs and phonons are strongly coupled, the ket vector representing this coupled state is expressed as the direct product \otimes of the electron state and the phonon state [7]. Here, el and phonon represent electrons and phonons,

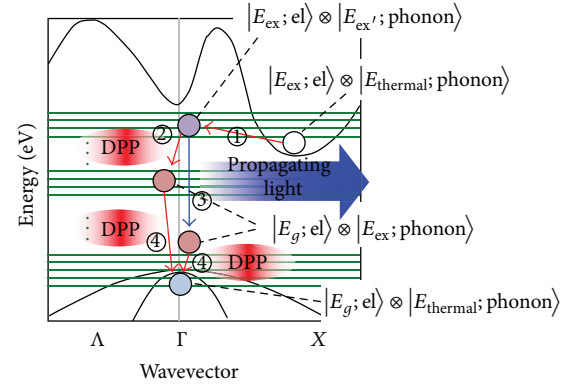


FIGURE 1: Light emission process via DPPs.

respectively, g represents the ground state, thermal represents thermal equilibrium, and ex and ex' represent excited states. First, the initial state is formed by injection of carriers from outside. In this initial state, since the electrons are in the excited state, and the phonons are in the thermal equilibrium state determined by the crystal lattice temperature, we have $|E_{ex}; el\rangle \otimes |E_{thermal}; phonon\rangle$. In this state, light emission is obtained via a process in which electrons transition to the ground state $|E_g; el\rangle \otimes |E_{thermal}; phonon\rangle$, that is to say, a process in which they transition to the valence band. This transition occurs via the intermediate states $|E_{ex}; el\rangle \otimes |E_{ex}'; phonon\rangle$ and $|E_g; el\rangle \otimes |E_{ex}; phonon\rangle$. Since transitions to the ground state via these intermediate states are electric-dipole-allowed transitions, not only are DPPs generated (Figure 1, ① \rightarrow ② \rightarrow ④), but so is propagating light (Figure 1, ① \rightarrow ③ \rightarrow ④). In addition, because of the multimode coherent phonons involved in this process, photon emission with an energy different from E_g is possible. An inverse process to this process, in other words, an absorption process due to DPPs, also exists.

Next, a processing method is described. In an indirect transition type semiconductor, since phonon absorption/emission is necessary during the emission of a photon, the radiative recombination probability is extremely low. However, in the light-emission process via DPPs, since the DP couples with multimode coherent phonons, the radiative recombination probability is high. In other words, an LED can be realized by exciting electrons to the conduction band with current injection and by using the above-described phonon absorption/emission processes. Also, the light emission wavelength of this device depends not on E_g , but on the energy of the DPPs generated in the vicinity of the p-n junction. That is to say, emitted light having an energy higher than E_g can be obtained [13, 14]. The problem is that, in the case of a normal semiconductor crystal, the DPP generation probability inside the crystal is low, and it is difficult to bring about transitions via DPP intermediate states. Here, we explain how to form, in a self-organized manner, a nanostructure that readily generates DPPs.

First, p-type impurities are implanted into an n-type substrate to form a p-n junction. Next, while irradiating the p-n junction with laser light, a forward-bias current is made to

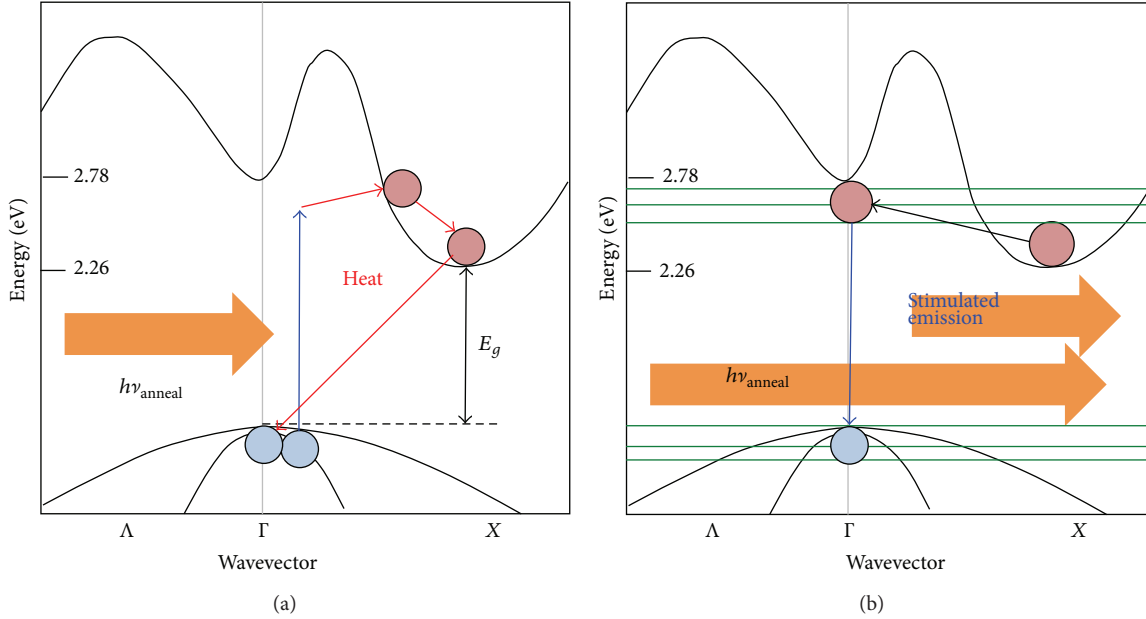


FIGURE 2: Principle of impurity diffusion by DPP-assisted annealing. (a) Heat generation due to light absorption. (b) Relative cooling due to stimulated emission.

flow to perform annealing. This processing method, known as DPP-assisted annealing [7, 12], changes the impurity distribution to a distribution suitable for generating DPPs. In the following, the processing principle is explained by dividing the distribution into a nanoregion that is not suitable for generating DPPs and a nanoregion that is suitable for generating DPPs.

(1) *Region Not Suitable for Generating DPPs.* If the photon energy of the irradiated laser light, $h\nu_{\text{laser}}$, is larger than E_g , as shown in Figure 2(a), an electron in the valence band absorbs a photon and is excited to the conduction band. This electron immediately emits a phonon due to intraband thermal relaxation and transitions to the bottom of the conduction band. Thermal energy $h\nu_{\text{laser}} - E_g$ is produced via this process. After relaxation, the electron-hole pair cannot undergo radiative recombination because of restrictions due to the wavenumber conservation law and instead undergoes nonradiative relaxation. Since this nonradiative relaxation also generates localized heat, all of the photon energy of the absorbed laser light is converted to thermal energy, causing dopant diffusion to proceed. As a result, Joule heating occurs due to the current, and heat generation occurs due to the nonradiative relaxation caused by the light irradiation.

(2) *Region Suitable for Generating DPPs.* Since a nonuniform domain boundary formed by the dopant (Zn) is formed inside the crystal by ion implantation at a high acceleration energy, the existence of a region that is suitable for generating DPPs locally can be expected. Let us assume that DPPs are generated around a certain Zn domain. In this case, as shown in Figure 2(b), at the electron-hole pairs, stimulated emission occurs via the DPP levels. As a result, unlike region (1), the locally absorbed energy is converted not only to thermal

energy but also to photon energy. Therefore, in the region around this Zn domain, heat generation is suppressed, and the diffusion rate is reduced.

In region (1), random diffusion continuously occurs, whereas in region (2), the diffusion rate is low. These diffusion processes continue until a structure suitable for generating DPPs is achieved. In addition, because the emitted light irradiates the whole device, it is not confined to the light-irradiation region but spreads in a self-organized manner throughout the whole device. When annealing is performed for a sufficiently long time, the concentration of Zn in the entire crystal is expected to take a spatial distribution that is optimal for stimulated emission via the DPP-assisted process. Moreover, since the probabilities of stimulated emission and spontaneous emission are proportional to each other [15], by using such a process, it is possible to realize an LED that emits photons.

3. Device Fabrication

The device fabrication process can be divided into two stages. First, a p-n homojunction structure is fabricated in a GaP single crystal by ion implantation. Then, the impurity distribution is altered by DPP-assisted annealing. The details of these are given below.

In the experiments performed in this study, we used an n-type (dopant: S) GaP single-crystal wafer with a thickness of $500\ \mu\text{m}$ and a diameter of 50 mm, grown by the liquid encapsulated Czochralski (LEC) method. The orientation was (111), and the dopant concentration was 2×10^{17} to $4 \times 10^{17}/\text{cm}^3$ (resistivity, $0.05\ \Omega\text{cm}$). This wafer was subjected to ion implantation to implant acceptors (Zn ions) with an implantation energy of 300 keV and a dose of $1.7 \times 10^{14}/\text{cm}^2$ to fabricate a p-n homojunction structure. By

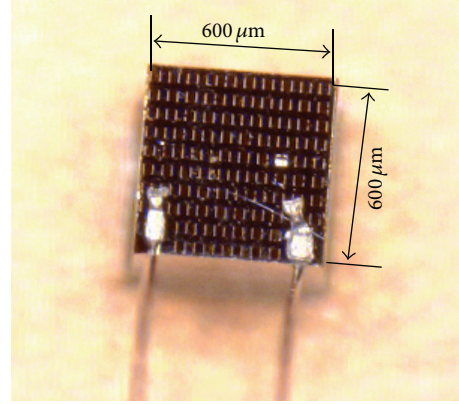
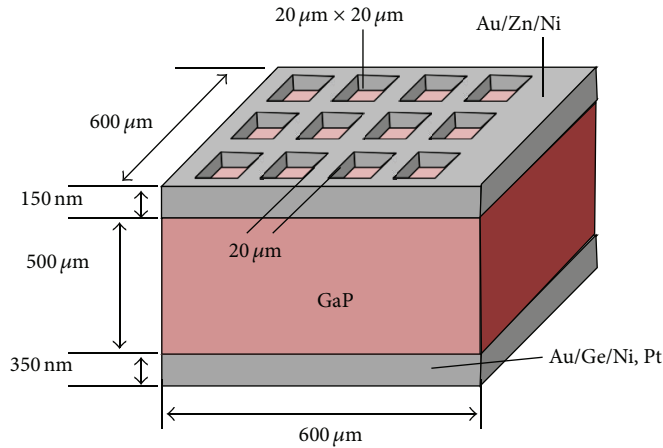


FIGURE 3: Schematic diagram of device and photograph of completed device.

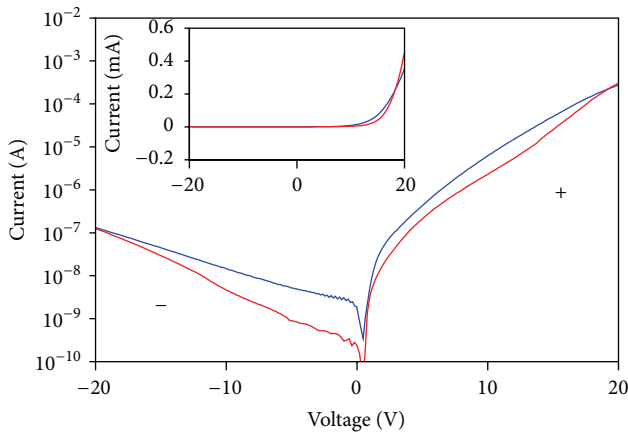


FIGURE 4: I - V characteristic of fabricated device. Red curve: before DPP-assisted annealing. Blue curve: after DPP-assisted annealing.

using such a high acceleration energy, a nonuniform domain boundary was formed, which was expected to form a region suitable for generating DPPs in a localized manner. After ion implantation, the surface was rinsed with HCl to remove excess Zn ions. After this, an Au/Zn/Ni film (150 nm) was deposited on the front surface (p-type side) of the substrate by sputtering and lift-off processing (Figure 3). The electrodes were formed in the shape of a mesh so as to facilitate light irradiation and light emission during DPP-assisted annealing and device driving, respectively. An Au/Ge/Ni film (300 nm) and a Pt film (50 nm) were sequentially deposited on the rear surface (n-type side) to serve as a negative electrode. Then, the wafer was diced into a $600\ \mu\text{m} \times 600\ \mu\text{m}$ chip and was fixed to a $20\ \text{mm} \times 20\ \text{mm} \times 1.7\ \text{mm}$ printed circuit board (PCB) by soldering the negative electrode. Finally, the positive electrode was connected to the PCB by wire bonding. The I - V characteristic of the fabricated device is shown in Figure 4 by the red curve. A rectification property was observed, indicating that a p-n junction was formed.

Next, the DPP-assisted annealing will be explained. Figure 5 shows the experimental setup used for DPP-assisted

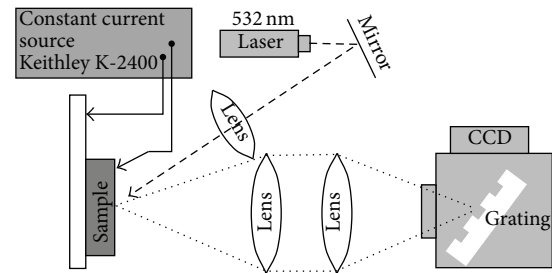


FIGURE 5: Experimental setup for DPP-assisted annealing and EL spectral measurements.

annealing and for measuring the EL spectrum. A K-2400 sourcemeter (Keithley Instruments Inc.) was used as a constant-current source for supplying current during the DPP-assisted annealing and during driving of the device. The emission spectrum of the device was measured using a spectrophotometer and a cooled Si-CCD (Roper Scientific Inc.). To make the device emit light in the green band (wavelengths around 530 nm), a forward-bias current of 30 mA ($9.9\ \text{A}/\text{cm}^2$) was applied to the device fabricated as described above while irradiating it with 532 nm wavelength ($2.32\ \text{eV}$) laser (DPSS CW laser, CNI Inc.) light. The laser power was 0.4 W, and the focal spot diameter on the surface of the device was $0.6\ \text{mm}$ ($35.4\ \text{W}/\text{cm}^2$). During the DPP-assisted annealing, the surface temperature of the device reached 40°C , while the PCB had been cooled to 26°C . As described in Section 2, the spatial distribution of the Zn ions was modified by Joule heat due to the current and by heat generated due to light absorption. The spectrum was measured every 1 hour. The processing was completed when the change in spectral intensity relative to the previous measurement was 1% or less.

4. Device Operation

4.1. Changes in Electroluminescence Spectrum due to DPP-Assisted Annealing. Figure 6(a) shows the results of

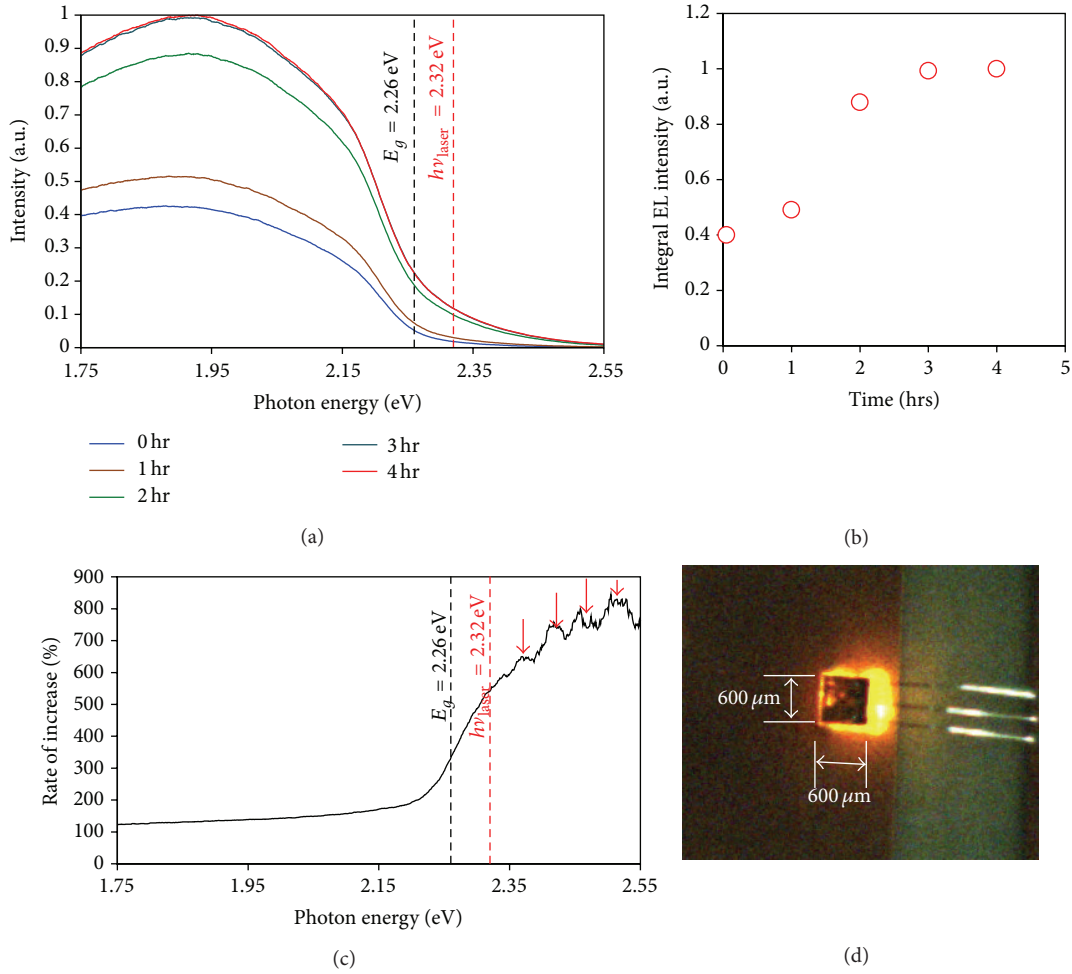


FIGURE 6: Temporal changes in EL spectra during DPP-assisted annealing of GaP LED. (a) Spectra observed during DPP-assisted annealing with a current density of 9.9 A/cm^2 while irradiating device with 532 nm laser light with power of 0.4 W. EL measurements were performed every 1 hour under the same current density conditions (9.9 A/cm^2), but without laser irradiation. (b) Total EL light emission intensity (integral of curve in (a)) versus time. (c) Measured values of R . (d) Light emission from fabricated device.

measuring the EL spectrum of the device during DPP-assisted annealing. The injection current was 30 mA. For reference, the photon energy of the irradiation light (2.32 eV) during DPP-assisted annealing and the bandgap energy of GaP (2.26 eV) are also shown by the vertical red and black dotted lines, respectively. The spectra were measured during an exposure time of 0.25 s, after the laser light irradiation was stopped. This figure shows that the light emission in the range 1.75–2.26 eV has become more intense as the annealing time was increased. Possible explanations for this include light emission from Zn-O pairs formed from Zn atoms and impurity O atoms which occupy the closely spaced Ga site and P site, respectively [16], and light emission originating from radiative recombination of electrons trapped at the donors (S) and free holes [17]. In particular, it has been reported that formation of Zn-O pairs can be explained by diffusion of Zn from the p side to the n side of the p-n junction [18]. In other words, the strong emission intensity in this region as DPP-assisted annealing progressed can be considered evidence that Zn diffusion took place. In

addition, light emission was observed from levels above E_g . This was a result of the DPP-assisted process described in Section 2. And the increase in light emission from these high energy levels was a result of the DPP-assisted annealing described also in Section 2.

Figure 6(b) shows the dependence of the total EL light emission intensity (the areas enclosed by the curves and the horizontal axis in Figure 6(a)) on the DPP-assisted annealing time. The light emission intensity saturated after about 3 hours of annealing, reaching an intensity three-times higher than the initial intensity.

Figure 6(c) shows the rate of increase R . It is the normalized emitted light intensity P of the photon energy E after saturation (after 4 hours of DPP-assisted annealing), given by the following expression:

$$R = \frac{P_{4\text{hr}}(E) - P_{0\text{hr}}(E)}{P_{0\text{hr}}(E)}. \quad (1)$$

In this figure, at photon energies below 2.2 eV ($< E_g$), R was 150–250%, whereas at photon energies higher than that of

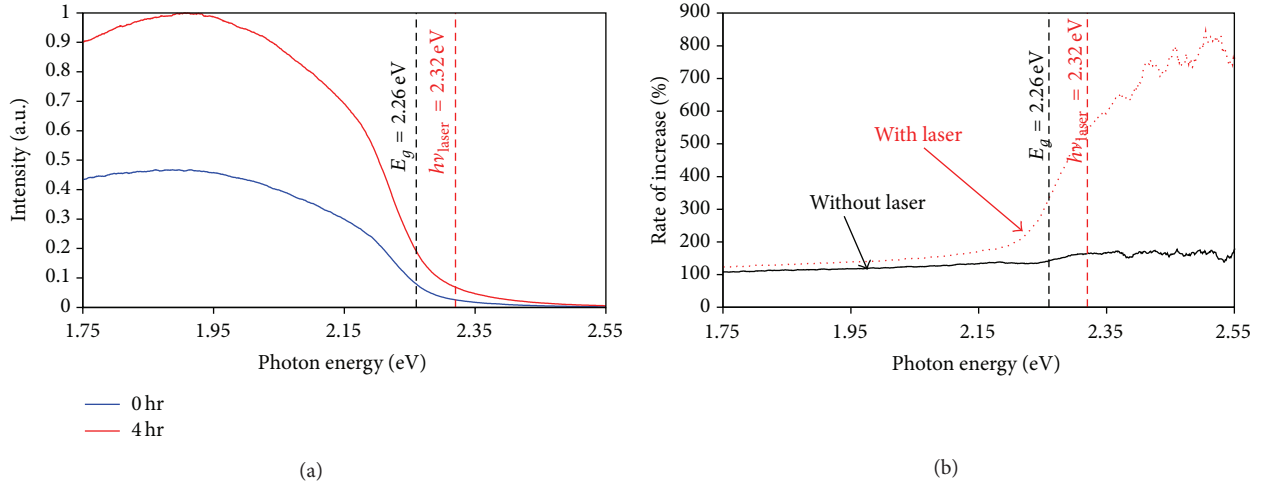


FIGURE 7: Spectrum of device annealed for 4 hours while applying current density of 9.9 A/cm^2 but no laser irradiation. (a) Blue curve shows initial spectrum, and red curve shows spectrum after DPP-assisted annealing for 4 hours. (b) Measured values of R . For comparison with case where annealing was performed without laser irradiation (black curve), the case where annealing was performed with laser irradiation is also shown (Figure 6(c), red curve).

the irradiation laser light ($h\nu_{\text{laser}}$), R was 550% or greater. This intensity variation is in agreement with that expected from the discussion in Section 2. In addition, in this figure, periodic peaks (indicated by downward red arrows) are observed at positions away from $h\nu_{\text{laser}}$ ($=2.32$ eV). These peaks were 50 meV apart, which corresponds to the energy of LO phonons in GaP. In other words, phonon sidebands appeared in the emitted light in the high-energy region, as reported in a previous study [19, 20], confirming that the light emission phenomenon was due to a DPP-assisted process via multimode coherent phonons.

Figure 6(d) is a photomicrograph showing light emission from the device. Although the value of R was large at energies higher than the photon energy of the irradiation laser light ($h\nu_{\text{laser}}$), the emission component originating from impurities or Zn-O centers [16, 17] was strong, making the emitted light appear orange.

4.2. Effect of Photon Number Density on the DPP-Assisted Annealing. Usually, GaP contains defects or impurities such as oxygen, and these form emission centers. In other words, photons with a wide range of energies are generated inside the crystal during DPP-assisted annealing, and it is thought that stimulated emission is also made possible triggered by these generated photons.

To confirm the effect of this light emission inside the crystal, we performed annealing while causing a current to flow (30 mA), but without laser irradiation. The EL spectrum obtained as a result is shown in Figure 7(a). The black curve in Figure 7(b) is the rate of increase, R , given by (1) (the red curve is a copy of Figure 6(c)). First, the values of this black curve at the low energy side were close to the values of the red curve. However, above E_g , they considerably differed. This feature can be explained as follows. In the 1.7–2.2 eV energy band, the photon number density with the corresponding energy is the same, regardless of whether or

not laser irradiation is performed, and therefore, no change occurs in the DPP-assisted process. In addition, the light emission from Zn-O or defects does not change compared with the case where laser irradiation is performed, and therefore, the rate of increase is substantially the same. In the case of the high-energy band, it is thought that there is a difference between progression and suppression of dopant diffusion depending on whether or not laser irradiation is performed. In other words, if monochromatic light of sufficient intensity is made incident, stimulated emission from an energy level corresponding to the photon energy of that monochromatic light becomes more pronounced. Therefore, this demonstrates the effectiveness of DPP-assisted annealing, in terms of the ability to control the photon energy of the light emission from the device by the photon energy, $h\nu_{\text{laser}}$, of the irradiation light rather than E_g .

4.3. The Influence of Crystallinity. In general, lattice defects occur in crystals due to impurity doping by ion implantation. In particular, with high-energy ion implantation, there is also a risk of the crystal becoming amorphous. In the present study, light emission was brought about by a DPP-assisted process. However, this process uses high energy during ion implantation, and there is also a study in which a light-emitting device was fabricated using amorphous GaP [21]; therefore, we examined the crystallinity and its influence on light emission.

We used a sample that was preliminarily annealed at 800°C for 30 minutes prior to DPP-assisted annealing, after ion implantation. Figure 8 shows the measured Raman scattering spectra (incident light: 488 nm) of the substrate before ion implantation (blue circles), the substrate after ion implantation (red diamonds), and the substrate after preliminary annealing carried out in a furnace (green triangles). In the spectrum for the substrate before ion implantation, sharp peaks appeared, which indicate the high crystal

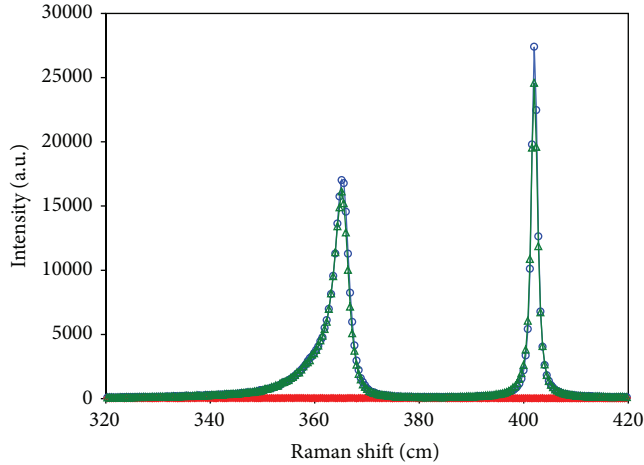


FIGURE 8: Measured Raman scattering spectra. Blue circles: substrate before ion implantation, for comparison. Red diamonds: substrate after ion implantation. Green triangles: substrate subjected to preliminary annealing after ion implantation (800°C, 30 minutes).

quality. However, after ion implantation, these peaks were not observed; therefore, it is considered that the surface changed to an amorphous structure. Also, in the spectrum for the substrate after preliminary annealing, peaks appeared again. To confirm the effect of the amorphous surface on light emission, the substrate whose surface crystallinity was restored by preliminary annealing was formed into a device and was subjected to DPP-assisted annealing under the same conditions. The results are shown in Figure 9. As can be understood from this figure, the same spectral change as shown in Figures 6(a) and 6(c) was observed also in the preannealed sample.

The results shown in Figures 8 and 9 can be explained as follows: by implanting Zn into GaP with a high acceleration energy, namely, 300 keV, the surface of the GaP crystal became amorphous. However, via the DPP-assisted process, the light emission occurs at the domain boundaries formed by the dopant (Zn) inside the crystal and does not rely on the amorphization of the crystal surface. Thus, the same results are obtained regardless of whether or not preliminary annealing is performed to recover the crystallinity.

5. Conclusion

We successfully fabricated a light-emitting device by forming a p-n junction via ion implantation in a bulk GaP crystal, which is an indirect-transition type semiconductor, and by using DPP-assisted annealing. The EL spectrum of the device fabricated by this method was governed by the light used during processing, not by the band structure of the semiconductor. In practice, the light emission from energy levels higher than 2.32 eV was increased by more than 550% (E_g of GaP is 2.26 eV) by using 532 nm (2.32 eV) light irradiation during the DPP-assisted annealing. In contrast, the rate of increase in the energy region below 2.2 eV was limited to 150–250%. By performing experiments with and without

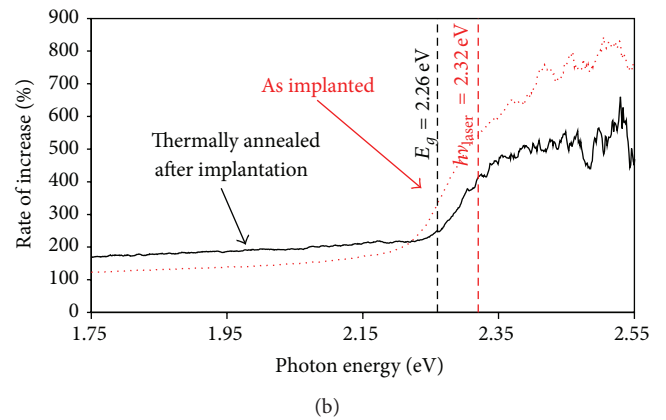
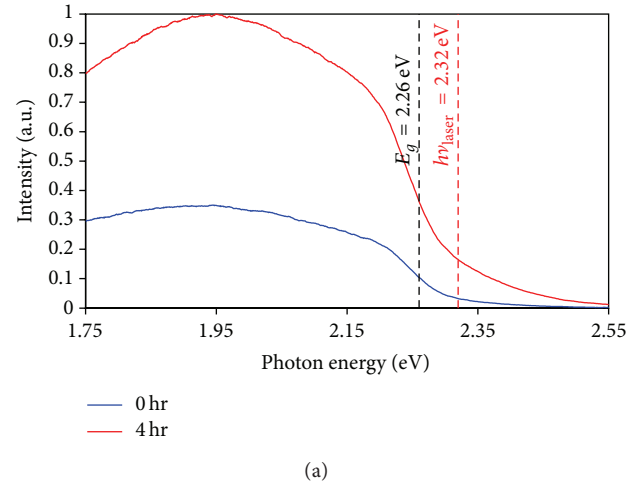


FIGURE 9: Results of DPP-assisted annealing of sample subjected to preliminary annealing after ion implantation. Processing was performed under the same conditions as in Figure 6 (applying current density of 9.9 A/cm² while irradiating the device with 532 nm laser light at power of 0.4 W). (a) Comparison of initial spectrum and spectrum obtained at saturation. (b) Rate of increase of EL spectral intensity (black solid curve). Case without preliminary annealing is also shown for comparison (Figure 6(c), red curve).

irradiation light, we also observed a phenomenon whereby the light emission intensity from higher energy levels was increased as a result of the DPP-assisted annealing, thus demonstrating the effectiveness of the DPP-assisted process. In addition, it was also confirmed experimentally that this light was emitted from a single crystal and was not due to amorphization.

Although the light emission from energy levels higher than E_g was remarkably increased, the peak position of the EL spectrum was around 630 nm due to defects and impurity O atoms. Thus, we believe that it will be possible to realize a GaP LED with an emission peak around 530 nm, provided that the crystallinity of the GaP can be improved.

Conflict of Interests

The authors declare that there is no conflict of interests regarding the publication of this paper.

Acknowledgments

The authors received support in Raman spectroscopy from Professor Dr. S. Takagi, Professor Dr. M. Takenaka, and Mr. J.-H. Han of The University of Tokyo. This work was partially supported by a Grant-in-Aid for Scientific Research (B) (no. 24360023) of MEXT and Core-to-Core Program of JSPS.

References

- [1] IARC *Monographs on the Evaluation of Carcinogenic Risks to Humans*, vol. 23 of *Some Metals and Metallic Compounds*, World Health Organization, International Agency for Research on Cancer, 1998.
- [2] M. Behet, R. Hövel, A. Kohl, A. Mesquida Küsters, B. Opitz, and K. Heime, "MOVPE growth of III-V compounds for optoelectronic and electronic applications," *Microelectronics Journal*, vol. 27, no. 4-5, pp. 297-334, 1996.
- [3] P. Fini, X. Wu, E. J. Tarsa et al., "The effect of growth environment on the morphological and extended defect evolution in GaN grown by metalorganic chemical vapor deposition," *Japanese Journal of Applied Physics Part 1*, vol. 37, no. 8, pp. 4460-4466, 1998.
- [4] D. D. Koleske, A. E. Wickenden, R. L. Henry, W. J. DeSisto, and R. J. Gorman, "Growth model for GaN with comparison to structural, optical, and electrical properties," *Journal of Applied Physics*, vol. 84, no. 4, pp. 1998-2010, 1998.
- [5] P. Gibart, "Metal organic vapour phase epitaxy of GaN and lateral overgrowth," *Reports on Progress in Physics*, vol. 67, no. 5, pp. 667-715, 2004.
- [6] Y. Tanaka and K. Kobayashi, "Optical near field dressed by localized and coherent phonons," *Journal of Microscopy*, vol. 229, no. 2, pp. 228-232, 2008.
- [7] M. Ohtsu, "Dressed photon technology," *Nanophotonics*, vol. 1, pp. 83-97, 2012.
- [8] M. Gershenson and R. M. Mikulyak, "Light emission from forward biased p-n junctions in gallium phosphide," *Solid State Electronics*, vol. 5, no. 5, pp. 313-329, 1962.
- [9] D. G. Thomas, M. Gershenson, and F. A. Trumbore, "Pair spectra and "edge" emission in gallium phosphide," *Physical Review*, vol. 133, no. 1, pp. A269-A279, 1964.
- [10] R. A. Logan, H. G. White, and W. Wiegmann, "Efficient green electroluminescent junctions in GaP," *Solid State Electronics*, vol. 14, no. 1, pp. 55-70, 1971.
- [11] J. S. Jayson, R. Z. Bachrach, P. D. Dapkus, and N. E. Schumaker, "Evaluation of the Zn-O complex and oxygen-donor electron-capture cross sections in p-Type GaP: limits on the quantum efficiency of red-emitting (Zn,O)-doped material," *Physical Review B*, vol. 6, no. 6, pp. 2357-2372, 1972.
- [12] T. Kawazoe, M. A. Mueed, and M. Ohtsu, "Highly efficient and broadband Si homojunction structured near-infrared light emitting diodes based on the phonon-assisted optical near-field process," *Applied Physics B: Lasers and Optics*, vol. 104, no. 4, pp. 747-754, 2011.
- [13] M. A. Tran, T. Kawazoe, and M. Ohtsu, "Fabrication of a bulk silicon p-n homojunction-structured light-emitting diode showing visible electroluminescence at room temperature," *Applied Physics A*, vol. 115, no. 1, pp. 105-111, 2014.
- [14] T. Kawazoe and M. Ohtsu, "Bulk crystal SiC blue LED with p-n homojunction structure fabricated by dressed-photon-phonon-assisted annealing," *Applied Physics A*, vol. 115, no. 1, pp. 127-133, 2014.
- [15] A. Einstein and P. Ehrenfest, "Zur Quantentheorie des Strahlungsgleichgewichts," *Zeitschrift für Physik*, vol. 19, no. 1, pp. 301-306, 1923.
- [16] K. Löhnert and E. Kubalek, "On the degradation of electroluminescence efficiency in gallium phosphide green light emitting diodes," *Physica Status Solidi A*, vol. 80, no. 1, pp. 173-183, 1983.
- [17] T. Kawabata and S. Koike, "High-efficiency GaP pure green light-emitting diodes of 555 nm fabricated by new liquid phase epitaxy method," *Applied Physics Letters*, vol. 43, no. 5, pp. 490-491, 1983.
- [18] K. Ždánky, J. Zavadil, D. Nohavica, and S. Kugler, "Degradation of commercial high-brightness GaP:N green light emitting diodes," *Journal of Applied Physics*, vol. 83, no. 12, pp. 7678-7684, 1998.
- [19] M. Yamaguchi, T. Kawazoe, and M. Ohtsu, "Evaluating the coupling strength of electron-hole pairs and phonons in a 0.9 μm -wavelength silicon light emitting diode using dressed-photon-phonons," *Applied Physics A*, vol. 115, no. 1, pp. 119-125, 2014.
- [20] N. Wada, M. A. Tran, T. Kawazoe, and M. Ohtsu, "Measurement of multimode coherent phonons in nanometric spaces in a homojunction-structured silicon light emitting diode," *Applied Physics A: Materials Science and Processing*, vol. 115, no. 1, pp. 113-118, 2014.
- [21] K. Tomioka and S. Adachi, "Structural and photoluminescence properties of porous GaP formed by electrochemical etching," *Journal of Applied Physics*, vol. 98, no. 7, Article ID 073511, 2005.

Research Article

Realization of Ultraflat Plastic Film Using Dressed-Photon-Phonon-Assisted Selective Etching of Nanoscale Structures

Takashi Yatsui, Wataru Nomura, and Motoichi Ohtsu

School of Engineering, The University of Tokyo, 2-11-16 Yayoi, Bunkyo-ku, Tokyo 113-8656, Japan

Correspondence should be addressed to Takashi Yatsui; yatsui@ee.t.u-tokyo.ac.jp

Received 30 September 2014; Accepted 6 November 2014

Academic Editor: Chennupati Jagadish

Copyright © 2015 Takashi Yatsui et al. This is an open access article distributed under the Creative Commons Attribution License, which permits unrestricted use, distribution, and reproduction in any medium, provided the original work is properly cited.

We compared dressed-photon-phonon (DPP) etching to conventional photochemical etching and, using a numerical analysis of topographic images of the resultant etched polymethyl methacrylate (PMMA) substrate, we determined that the DPP etching resulted in the selective etching of smaller scale structures in comparison with the conventional photochemical etching. We investigated the wavelength dependence of the PMMA substrate etching using an O₂ gas. As the dissociation energy of O₂ is 5.12 eV, we applied a continuous-wave (CW) He-Cd laser ($\lambda = 325$ nm, 3.81 eV) for the DPP etching and a 5th-harmonic Nd:YAG laser ($\lambda = 213$ nm, 5.82 eV) for the conventional photochemical etching. From the obtained atomic force microscope images, we confirmed a reduction in surface roughness, R_a , in both cases. However, based on calculations involving the standard deviation of the height difference function, we confirmed that the conventional photochemical etching method etched the larger scale structures only, while the DPP etching process selectively etched the smaller scale features.

1. Introduction

Organic materials are flexible in comparison with inorganic substrates; therefore, they are important materials as regards the development of future wearable devices [1]. Recently, organic substrates with microstructures have been prepared by mechanical pressing, an injection molding method [2], and the surface roughness values of the obtained materials have been determined by use of a pressing mold. However, because the resultant plastic is soft, these organic substrates cannot be flattened using a mechanical polishing method. Furthermore, although plastic substrates are easy to fabricate in three-dimensional structures, the side walls of these structures cannot be flattened.

In order to achieve an ultraflat surface on an inorganic material, many groups have developed a chemical mechanical polishing (CMP) method [3], resulting in a subnanometer scale flattened surface [4]. However, since CMP is a contact method, it leads to the formation of scratches or digs during polishing, while chemical materials in the slurry penetrate the polished surface, resulting in performance degradation.

Therefore, we have developed a dressed-photon-phonon (DPP) etching technique [5] as a noncontact flattening method. In this process, the free photons of propagating light are coupled with material excitation, including electrons and holes, of the nanoscale material structures; in other words, the photons interacting with the nanoscale material dress the material excitation to form a dressed photon (DP) quasiparticle. The DP also couples with multiple-mode coherent phonons in the material, which act as quasiparticle of DP and phonons (DPP). Therefore, the DPP energy is higher than that of the incident free photon; that is, the DPP realizes energy upconversion [6]. By using the energy upconversion mechanism, selective etching of the nanoscale structure can be successfully realized. Previously, we obtained ultraflat surfaces on substrates including glass [5], diamond, and GaN [7]. Since DPP etching does not require a contact pad, three-dimensional structures have also been flattened [8].

Here, we compare the effectiveness of the DPP etching technique to that of conventional photochemical etching. To evaluate the effectiveness of the DPP etching, we perform

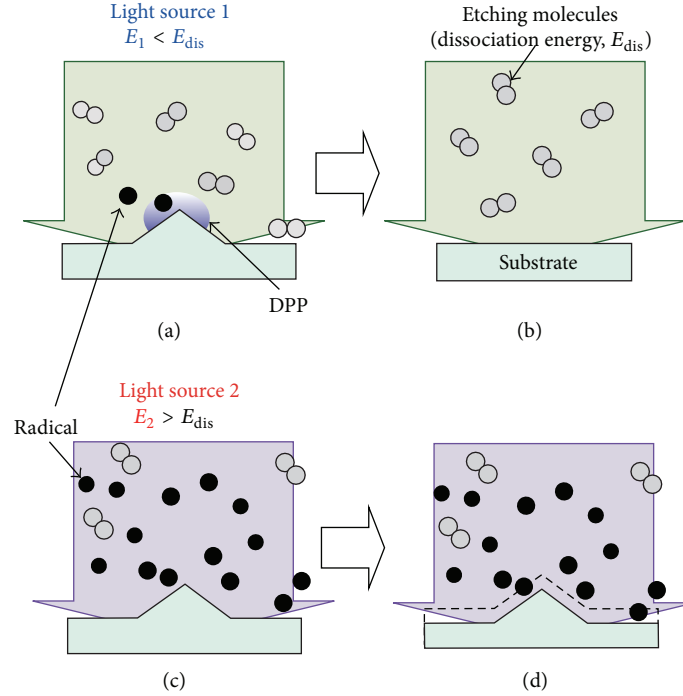


FIGURE 1: ((a) and (b)) DPP etching and ((c) and (d)) conventional photochemical etching process diagrams.

calculations based on the standard deviation of the height difference function in addition to the surface roughness, R_a . Here, we observe the wavelength dependence of photochemical etching on polymethyl methacrylate (PMMA) substrate as a plastic material.

2. DPP Etching

To realize DPP etching, the photon energy of the light source, E_1 , must be lower than the dissociation energy of the etching molecule, E_{dis} . Therefore, the incident photon cannot dissociate the etching molecules in a gas phase. However, the DPP is generated at the apex of the protrusions of the surface. Furthermore, since the DPP energy, E_{DPP} , is larger than that of E_1 , the etching molecules are dissociated selectively when they enter the proximity of the protrusions (Figure 1(a)). Consequently, the dissociated radical molecules etch away at the protrusions and, thus, the DPP etching process automatically stops when the surface is sufficiently flattened (Figure 1(b)).

In contrast to DPP etching, when conventional plasma etching or conventional photochemical etching is used, the photon energy of the light source, E_2 , is higher than E_{dis} , and the etching molecules are dissociated in all directions (Figure 1(c)). Therefore, the dissociated radical atoms etch the substrate with no position dependence (Figure 1(d)).

3. Experiment

In this study, we used a PMMA substrate prepared by injection molding in an oxygen atmosphere. Because the dissociation

energy of O_2 is 5.12 eV [9], we used a continuous-wave (CW) He-Cd laser ($\lambda = 325$ nm; 3.81 eV; excitation power: 0.8 W/cm²) for DPP etching and a 5th-harmonic YAG laser ($\lambda = 213$ nm; 5.82 eV; 20 Hz; pulse width: 5 ns) for conventional photochemical etching. The surface structure was evaluated using an atomic force microscope (AFM) with a “sampling intelligent scan” mode (Hitachi-Hitech-Science Corp.). The scanned area was 1×1 μ m and incorporated 256×256 pixels (a spatial resolution of 4 nm) and the AFM images were obtained using tilt compensation and the third-order least-squares method.

4. Results and Discussion

Figures 2(a) and 2(b) are AFM images of the surface before and after DPP etching, respectively. It was found that the surface roughness, R_a , was reduced from 0.30 to 0.22 nm following 120 min DPP etching (Figure 3). Similar R_a reduction was observed following conventional photochemical etching, as can be seen from the AFM images taken before (Figure 2(c), $R_a = 0.26$ nm) and after (Figure 2(d), $R_a = 0.20$ nm) etching, and comparison between both methods is given in Figure 3. It can be seen that the usage of conventional photochemical etching resulted in a dramatic decrease in etching time.

To investigate the surface morphology in detail, we used the method developed in our previous reports [7]. Instead of examining the value of R_a only, which is the average value of the absolute surface height deviations from the best-fitting plane (Figure 4(a)), we used the standard deviation of the height difference function. Here, the R_a value

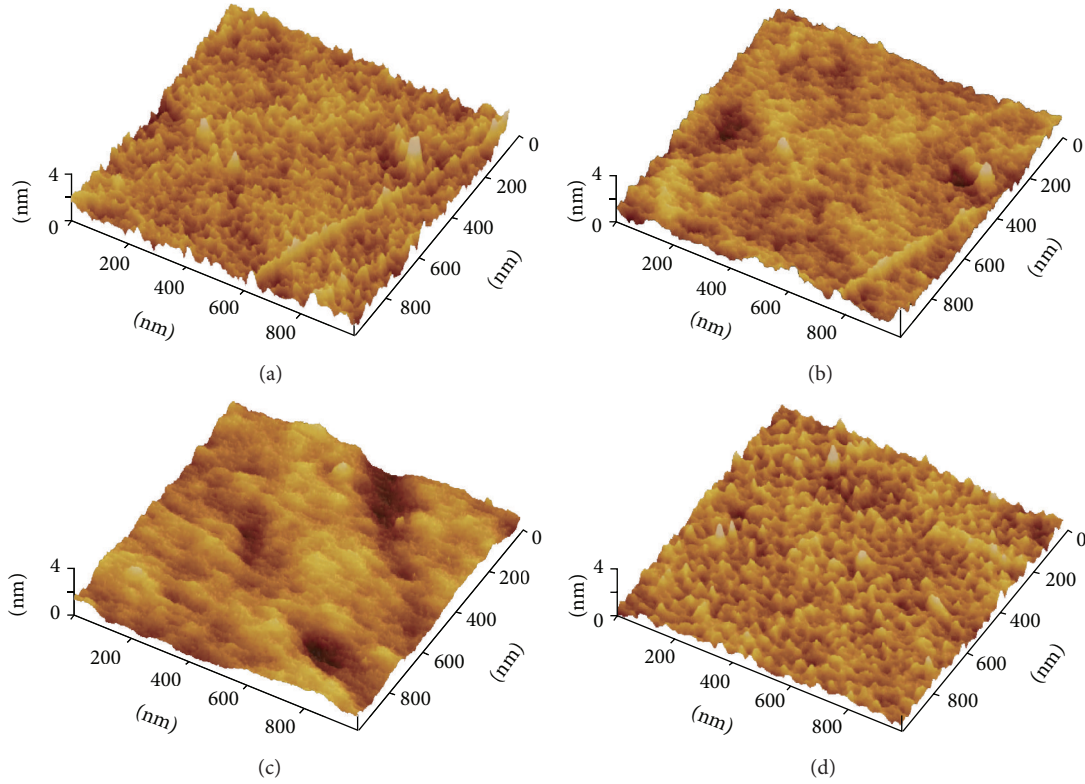


FIGURE 2: Typical AFM images of PMMA substrate (a) before and (b) after DPP etching using He-Cd laser ($\lambda = 325 \text{ nm}$, 3.81 eV). Typical AFM images of PMMA substrate (c) before and (d) after conventional photochemical etching using 5th-harmonic YAG laser ($\lambda = 213 \text{ nm}$, 5.82 eV).

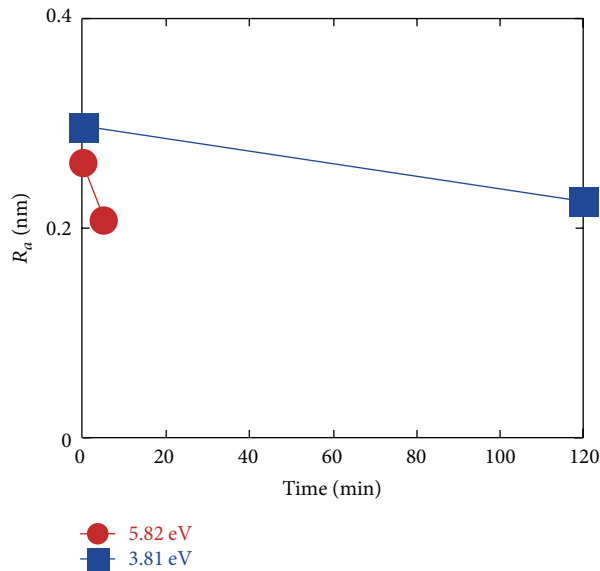


FIGURE 3: Etching time dependence of surface roughness, R_a . Blue solid squares correspond to R_a using 3.81 eV He-Cd laser (DPP etching). Red solid circles correspond to R_a using 5.82 eV 5th-harmonic Nd:YAG laser (conventional photochemical etching).

provides information about the average surface roughness for the entire scanning region. However, the standard deviation of the height difference function is given by $R(l) = \sqrt{\langle (z_{k+1}^{(l)} - z_k^{(l)})^2 / 2 \rangle}$, where l is the scale size, z is the height

from the best-fitting plane, and $\overline{z_k^{(l)}}$ is the average z value of the scale (Figure 4(b)) [10]. This $R(l)$ can be used to determine the contributions of the surface roughness values (at different length scales) to the overall surface roughness. As this value

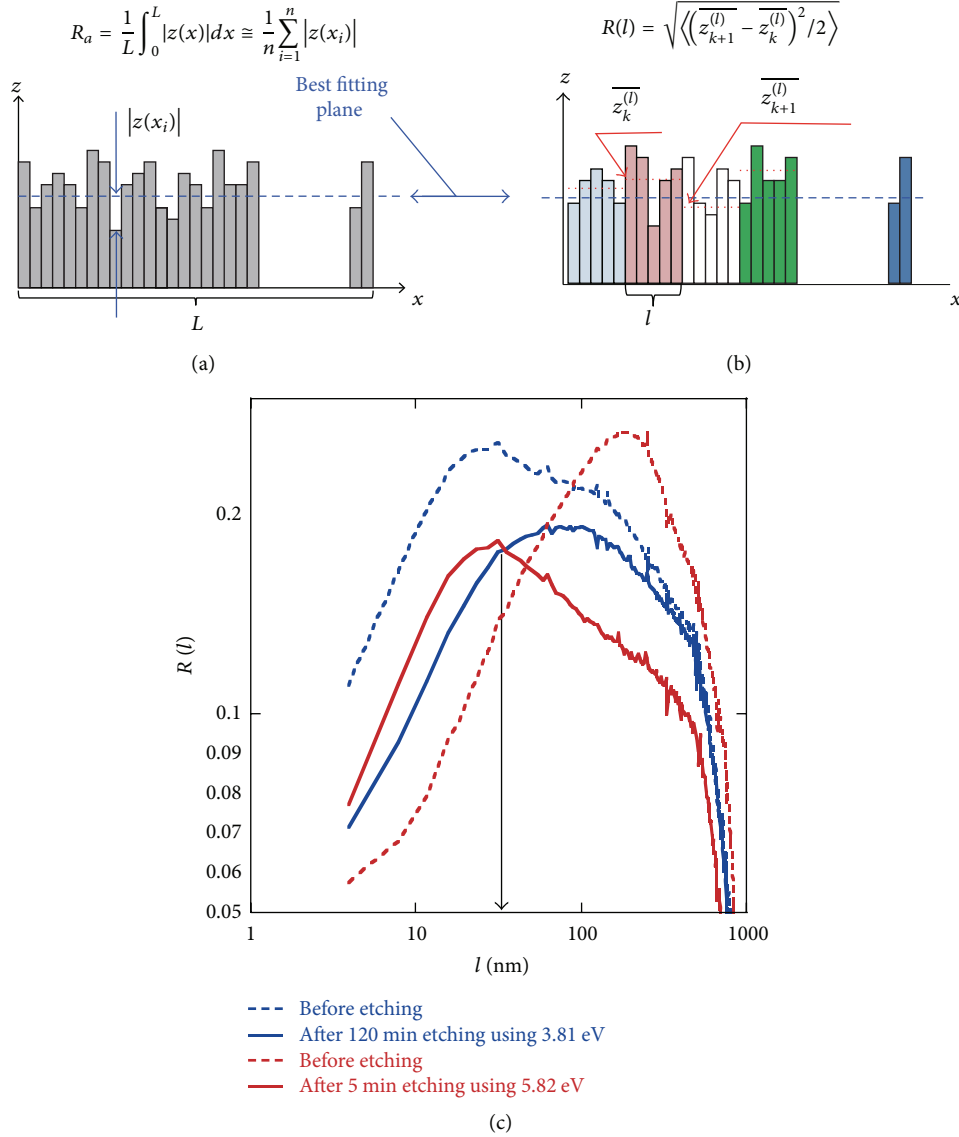


FIGURE 4: Schematic of (a) the surface roughness, R_a , and the standard deviation of the height difference function, $R(l)$. (c) Etching time dependence of the standard deviation of $R(l)$. The blue dashed curve corresponds to Figure 2(a) (before etching); the blue solid curve corresponds to Figure 2(b) (after 120 min etching using 3.81 eV DPP etching); the red dashed curve corresponds to Figure 2(c) (before etching); the red solid curve corresponds to Figure 2(d) (after 5 min etching using 5.82 eV conventional photochemical etching).

indicates the height difference of the next scale, it is known as a two-sample variance. This value is known as the Allan variance, and it is a measure of frequency stability in clocks, oscillators, and amplifiers.

Figure 4 shows the calculated $R(l)$ values from the AFM images. The maximum values of the blue curves decreased from 0.25 to 0.19 nm, which are comparable to the R_a values of Figure 2(a) (0.30 nm) and Figure 2(b) (0.22 nm) and indicate the results of the DPP etching. Similarly, the maximum values of the red curves decreased from 0.27 to 0.18 nm, which are comparable to the R_a values of Figure 2(c) (0.26 nm) and Figure 2(d) (0.20 nm) and are the photochemical etching results. It is notable that even though the R_a values vary significantly with each other, we can therefore confirm that the conventional etching etched on a scale, l , larger than

100 nm, while the DPP etching etched on a smaller scale, with l less than 100 nm. These results therefore establish that DPP etching selectively etches on a smaller scale, as the $R(l)$ value for the DPP etched is smaller than that of the conventional photochemical etching at $l < 35$ nm (indicated by the arrow in Figure 4). The increase in $R(l)$ at the smaller scale for the conventional photochemical etching case might be caused by ablation due to the higher photon energy used in this method, in comparison with that of the chemical bonding of PMMA [11].

5. Conclusion

Through an experiment on the wavelength-dependent etching of a polymethyl methacrylate (PMMA) substrate and

calculations based on the standard deviation of the height difference function of the resultant surface, we determined that dressed-photon-phonon (DPP) etching results in the selective etching of smaller scale structures in comparison with conventional photochemical etching. This information therefore supports the use of the DPP etching method for the surface finishing of organic materials. In future, by combining both DPP and conventional photochemical etching, a further decrease in the R_a value could be realized depending on the R_a value of the substance in question.

Conflict of Interests

The authors declare that there is no conflict of interests regarding the publication of this paper.

Acknowledgments

The authors wish to express special thanks to Dr. Takashi Morimoto and Mr. Yoshinori Tabata (SIGMA Koki Co., Ltd.) for their active support and discussions. This work was partially supported by a Grant-in-Aid for Scientific Research (B) (no. 26286022), the Exploratory Research program (no. 26630122) of MEXT, Core-to-Core Program of JSPS (A. Advanced Research Networks), and a research grant (Basic Research) from The Asahi Glass Foundation. They would like to thank Editage (<http://www.editage.jp/>) for English language editing.

References

- [1] M. Kaltenbrunner, T. Sekitani, J. Reeder et al., "An ultra-lightweight design for imperceptible plastic electronics," *Nature*, vol. 499, no. 7459, pp. 458–463, 2013.
- [2] B.-K. Lee, D. S. Kim, and T. H. Kwon, "Replication of microlens arrays by injection molding," *Microsystem Technologies*, vol. 10, no. 6-7, pp. 531–535, 2004.
- [3] L. Jianfeng and D. A. Dornfeld, "Material removal mechanism in chemical mechanical polishing: theory and modeling," *IEEE Transactions on Semiconductor Manufacturing*, vol. 14, no. 2, pp. 112–133, 2001.
- [4] A. J. Kadaksham, B. Lee, M. House, T. Laursen, B. Niekrewicz, and A. Rastegar, "Current status of EUV mask blanks and LTEM substrates defectivity and cleaning of blanks exposed in EUV ADT," in *Extreme Ultraviolet (EUV) Lithography II*, 79690Z, vol. 7969 of *Proceedings of SPIE*, San Jose, Calif, USA, February 2011.
- [5] T. Yatsui, K. Hirata, W. Nomura, Y. Tabata, and M. Ohtsu, "Realization of an ultra-flat silica surface with angstrom-scale average roughness using nonadiabatic optical near-field etching," *Applied Physics B: Lasers and Optics*, vol. 93, no. 1, pp. 55–57, 2008.
- [6] M. Ohtsu, "Dressed photon technology," *Nanophotonics*, vol. 1, pp. 83–97, 2012.
- [7] T. Yatsui, W. Nomura, F. Stehlin, O. Soppera, M. Naruse, and M. Ohtsu, "Challenges in realizing ultraflat materials surfaces," *Beilstein Journal of Nanotechnology*, vol. 4, no. 1, pp. 875–885, 2013.
- [8] T. Yatsui, D. Takeuchi, S. Koizumi et al., "Polarization-controlled dressed-photonphonon etching of patterned diamond structures," *Physica Status Solidi (A)*, vol. 211, no. 10, pp. 2339–2342, 2014.
- [9] D. Keilin and E. F. Hartree, "Absorption spectrum of oxygen," *Nature*, vol. 165, no. 4197, pp. 543–544, 1950.
- [10] D. W. Allan, "Statistics of atomic frequency standards," *Proceedings of the IEEE*, vol. 54, no. 2, pp. 221–230, 1966.
- [11] R. Srinivasan and B. Braren, "Ultraviolet laser ablation of organic polymers," *Chemical Reviews*, vol. 89, no. 6, pp. 1303–1316, 1989.

Research Article

Emission Spectral Control of a Silicon Light Emitting Diode Fabricated by Dressed-Photon-Phonon Assisted Annealing Using a Short Pulse Pair

Tadashi Kawazoe,^{1,2} Naoki Wada,¹ and Motoichi Ohtsu^{1,2}

¹ Department of Electrical Engineering and Information Systems, Graduate School of Engineering, The University of Tokyo, 2-11-16 Yayoi, Bunkyo-ku, Tokyo 113-8656, Japan

² Nanophotonic Research Center, Graduate School of Engineering, The University of Tokyo, 2-11-16 Yayoi, Bunkyo-ku, Tokyo 113-8656, Japan

Correspondence should be addressed to Tadashi Kawazoe; kawazoe@ee.t.u-tokyo.ac.jp

Received 24 April 2014; Accepted 5 June 2014; Published 6 July 2014

Academic Editor: Takashi Yatsui

Copyright © 2014 Tadashi Kawazoe et al. This is an open access article distributed under the Creative Commons Attribution License, which permits unrestricted use, distribution, and reproduction in any medium, provided the original work is properly cited.

We fabricated a high-efficiency infrared light emitting diode (LED) via dressed-photon-phonon (DPP) assisted annealing of a p-n homojunctioned bulk Si crystal. The center wavelength in the electroluminescence (EL) spectrum of this LED was determined by the wavelength of a CW laser used in the DPP-assisted annealing. We have proposed a novel method of controlling the EL spectral shape by additionally using a pulsed light source in order to control the number of phonons for the DPP-assisted annealing. In this method, the Si crystal is irradiated with a pair of pulses having an arrival time difference between them. The number of coherent phonons created is increased (reduced) by tuning (detuning) this time difference. A Si-LED was subjected to DPP-assisted annealing using a 1.3 μm ($h\nu = 0.94$ eV) CW laser and a mode-locked pulsed laser with a pulse width of 17 fs. When the number of phonons was increased, the EL emission spectrum broadened toward the high-energy side by 200 meV or more. The broadening towards the low-energy side was reduced to 120 meV.

1. Introduction

Direct transition type semiconductors are mainly used in semiconductor light emitting diodes (LEDs) [1, 2]. The reason for this is that the probability of electric dipole transitions, in other words, the radiative recombination probability, is high. Also, the emission wavelength is determined by the bandgap energy, E_g , of the material used. Therefore, for example, InGaAsP epitaxially grown on an InP substrate is mainly used as the active layer for near-infrared LEDs with emission wavelengths of 1.00–1.70 μm (0.73–1.24 eV), which includes the optical fiber communication wavelength band. Shortcomings with this approach are that InP is highly toxic [3], and In is a rare resource. Silicon (Si), on the other hand, is a semiconductor having low toxicity and no concerns about depletion of resources; however, its emission efficiency is low since it is an indirect transition type semiconductor.

Therefore, Si is usually not suitable as a material for use in LEDs. Nevertheless, there is a great demand for the use of Si in light emitting devices, and there has been extensive research into improving its emission efficiency. For example, there has been research into making Si emit light in the visible region by utilizing the quantum size effect of Si and by using porous Si [4], a Si/SiO₂ superlattice structure [5, 6], and Si nanoprecipitates in SiO₂ [7], as well as research into making Si emit light in the near-infrared region by doping it with light-emitting materials, such as erbium (Er)-doped Si [8] and silicon-germanium (Si-Ge) [9]. However, the reported external quantum efficiencies and power conversion efficiencies of LEDs using these materials have been low, at 0.5% and 0.8%, respectively [10].

On the other hand, using a homojunction-structured Si bulk crystal, we realized a high-efficiency, wideband LED in which the spatial distribution of the dopant density in

the Si was modified via a novel process of dressed-photon-phonon assisted annealing (DPP-assisted annealing) [11], and we achieved an external quantum efficiency of 40% and a power conversion efficiency of 50% [12]. A dressed photon (DP) is a quasi-particle created when a photon couples with an electron-hole pair in a nanometric region. Similarly, a dressed-photon-phonon (DPP) is a quasi-particle created when a DP couples with a phonon in a nanometric region. We have also succeeded in developing a Si laser [13], an infrared Si photodetector [14], and a Si relaxation oscillator [15], by using DPP-assisted annealing. These devices operate based on transitions mediated by DPPs, and the center wavelength of the electroluminescence (EL) spectrum is determined by the wavelength of the light source used for creating the DPPs. Since a DPP is a state in which a DP is coupled with a phonon in the material, the EL spectrum of the Si-LED described above has a large number of sidebands that are regularly arranged with a spacing corresponding to the optical phonon energy, centered on the photon energy of the light used in the DPP-assisted annealing. These sidebands are caused by coherent phonons (CPs) contributing to light emission. In typical light emitting devices, such sidebands originating from phonons (phonon sidebands) are observed in the photoluminescence spectrum, but are not observed in the EL spectrum. The observation of such sidebands in the EL spectrum, as described above, is a phenomenon unique to LEDs fabricated using DPPs. By using this phenomenon, it is possible to control the shape of the EL spectrum of a Si-LED by controlling the number of CPs created during the DPP-assisted annealing. In this paper, we report the results of our experiments in which we succeeded in controlling the generation of CPs by using a pair of pulses during the DPP-assisted annealing, allowing us to control the shape of the emission spectrum of a Si-LED.

2. Si-LED Fabrication and Principle of Sideband Creation

First, for fabricating a Si-LED, ion implantation is used to form an inhomogeneous spatial distribution of the dopant (boron: B) in a Si p-n homojunction substrate. Although the inhomogeneously concentrated B serves as the origin of the created DPPs, the created DPPs are not converted to propagating light that is detected outside the LED. However, if DPP-assisted annealing is used, it is possible to modify the spatial distribution of the B concentration so that the DPPs are converted to propagating light with high efficiency [12]. In the DPP-assisted annealing, a Si p-n homojunction substrate is irradiated with CW laser light while applying a forward-bias current, to control the thermal diffusion rate of the B. With this method, it has been demonstrated that the emission wavelength of a Si-LED does not depend on the bandgap energy, E_g , of the material used, but is determined by the photon energy, $h\nu_{\text{anneal}}$, of the radiated light [16]. In the present work, we performed DPP-assisted annealing by radiating CW laser light having a photon energy ($h\nu_{\text{anneal}} = 0.94$ eV) lower than E_g of silicon ($= 1.14$ eV). The principle will be described below. For more details, refer to [12].

During DPP-assisted annealing, the radiated light is not absorbed by the Si crystal at positions in the B distribution where DPPs are not created under irradiation. Thus, the energy of the electrons injected from the forward bias current is converted to thermal energy and is subsequently dissipated via intraband relaxation or nonradiative relaxation. Therefore, the B distribution randomly varies due to thermal diffusion. On the other hand, at positions where DPPs are readily created, the radiated light interacts with electron-hole pairs and phonons, whereby DPPs are created. In this case, the injected electrons emit propagating light via stimulated emission driven by localized DPPs. In other words, since part of the energy of the injected electrons is dissipated not in the form of thermal energy but in the form of optical energy, thermal diffusion becomes more difficult. In the two processes described above, the B concentration distribution in the Si crystal is modified, in a self-organized manner, to a structure suitable for the creation of DPPs and their subsequent conversion to propagating light, and then reaches an equilibrium state. The B distribution in this state is suitable for stimulated emission with the photon energy of the light irradiation, $h\nu_{\text{anneal}}$, and since the spontaneous emission probability is proportional to the stimulated emission probability, this p-n homojunction functions as a Si-LED that emits propagating light.

Next, the mechanism of sideband creation will be explained. Figure 1(a) is an energy level diagram showing electronic states in a Si-LED fabricated by DPP-assisted annealing, and Figure 1(b) is a diagram in which an intermediate DPP level has been added to the band structure. The state $|E_g; \text{el}\rangle \otimes |E_{\text{ex}}; \text{phonon}\rangle$ in the figure is a state represented by the direct product of the ground state $|E_g; \text{el}\rangle$ of the electron and the excited phonon state $|E_{\text{ex}}; \text{phonon}\rangle$. Transitions to this state $|E_g; \text{el}\rangle \otimes |E_{\text{ex}}; \text{phonon}\rangle$ have been shown to occur only due to absorption or emission of photons via DPPs [11]. When this is illustrated in the electronic band structure, it is a localized state in which DPP-mediated excitation can take place and, therefore, it is indicated by a constant-energy straight line (horizontal solid or broken line), as shown in Figure 1(b), due to wavenumber uncertainty. Although an adequate explanation of the conventional light emission process in Si-LEDs has been possible until now with only Figure 1(a), Figure 1(b) is also presented in the present paper to emphasize the significance of phonons. In the light emission process of Si-LEDs, since electrons are excited to the state $|E_{\text{ex}}; \text{el}\rangle$ by current injection, the initial state $|E_{\text{ex}}; \text{el}\rangle \otimes |E_{\text{ex}}^{\text{thermal}}; \text{phonon}\rangle$ in the light emission process exists close to the X point in the conduction band in Figure 1(b). Here, $|E_{\text{ex}}^{\text{thermal}}; \text{phonon}\rangle$ is the thermally excited state of the phonon. Similarly, since the final state $|E_g; \text{el}\rangle \otimes |E_{\text{ex}}^{\text{thermal}}; \text{phonon}\rangle$, reached after the light emission, corresponds to the energy state of holes created by the injected current, the state $|E_g; \text{el}\rangle$ concentrates in the vicinity of the Γ point at the top of the valence band. The state $|E_{\text{ex}}^{\text{thermal}}; \text{phonon}\rangle$ is limited to phonons that can exist at room temperature, according to Bose statistics. In other words, the states $|E_{\text{ex}}; \text{el}\rangle \otimes |E_{\text{ex}}^{\text{thermal}}; \text{phonon}\rangle$ and $|E_g; \text{el}\rangle \otimes |E_{\text{ex}}^{\text{thermal}}; \text{phonon}\rangle$ are the initial state and the final state in the usual indirect transition.

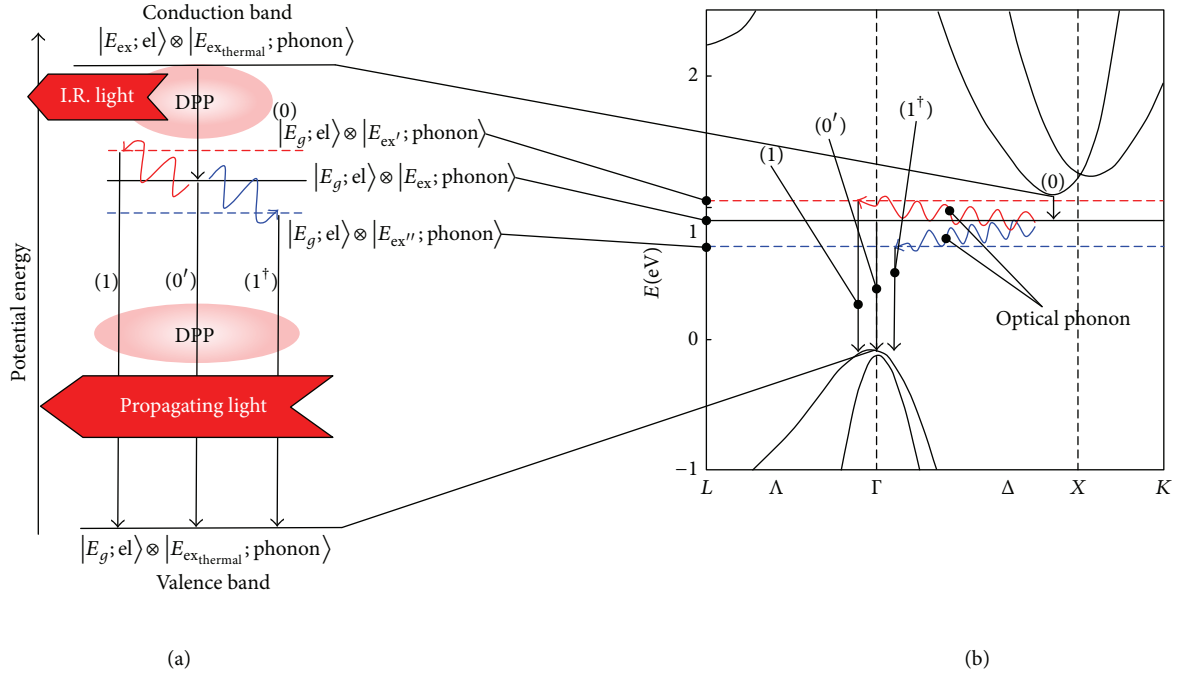


FIGURE 1: Diagram for explaining DPP-mediated transitions, showing (a) energy levels and (b) levels that can be reached via DPP-mediated transitions in electronic band structure of Si crystal.

Next, the processes (0), (0'), (1), and (1[†]) in Figure 1 will be explained. As the first-step, process (0) occurs. Processes (0'), (1), and (1[†]) occur as the second step. These processes involve externally observable transitions, in other words, photon emission. Processes (0) and (0') are transitions that do not require a phonon, whereas processes (1) and (1[†]) require an optical phonon. Similarly, (*n*) and (*n*[†]) are transitions involving *n* optical phonons (*n* = 2, 3, 4, ...).

Process (0) is the first-step transition from the initial state $|E_{ex}; el\rangle \otimes |E_{ex_{thermal}}; phonon\rangle$ of electrons injected near the X point by the current to the intermediate state $|E_g; el\rangle \otimes |E_{ex}; phonon\rangle$, which can be reached via a DPP-mediated transition. It corresponds to the energy relaxation from the bottom of the conduction band ($E_g = 1.14$ eV) to the state $|E_g; el\rangle \otimes |E_{ex}; phonon\rangle$ (in this paper, the energy of this state was experimentally determined to be 0.94 eV). This transition is allowable via emission of a large number of phonons or via the emission of infrared light. However, the probability of the transition via phonon emission is small because the simultaneous emission of about 10 phonons is required at room temperature (thermal energy 25 meV). On the other hand, in the transition via infrared light emission, since the electronic state changes from $|E_{ex}; el\rangle$ to $|E_g; el\rangle$, the selection rule required for photon emission is fulfilled. In addition, this transition is a direct transition in wavenumber space, as shown in Figure 1(b). Therefore, the probability of this transition is higher than the probability of a transition via phonon emission. In real space, this process is a transition from the state $|E_{ex}; el\rangle \otimes |E_{ex_{thermal}}; phonon\rangle$, which is broadened to the extent of the electron coherence length, to the localized state $|E_g; el\rangle \otimes |E_{ex}; phonon\rangle$. The reason why infrared light can be emitted in this transition is that part of

the electron energy can be dissipated as infrared light via a DPP having an energy that is resonant with this infrared light.

Process (0') is the second-step transition from the intermediate state $|E_g; el\rangle \otimes |E_{ex}; phonon\rangle$ to $|E_g; el\rangle \otimes |E_{ex_{thermal}}; phonon\rangle$. The photon energy emitted during this process is equal to $h\nu_{anneal}$. Since this is a transition between the same electronic states $|E_g; el\rangle$, the selection rule required for photon emission is governed by a phonon, and the state $|E_g; el\rangle \otimes |E_{ex}; phonon\rangle$ is also a state that can be reached via a DPP-mediated transition. The Si-LED fabricated by DPP-assisted annealing has a high probability of conversion from a DPP to propagating light, and almost all of the electrons in the state $|E_g; el\rangle \otimes |E_{ex}; phonon\rangle$ relax by emitting photons with energy $h\nu_{anneal}$.

Process (1) is the second-step transition from the intermediate state $|E_g; el\rangle \otimes |E_{ex}; phonon\rangle$ to the final state $|E_g; el\rangle \otimes |E_{ex_{thermal}}; phonon\rangle$ by absorption of an optical phonon. Since the first-step transition due to process (0) is an infrared light emission process, optical phonons are created via the Raman process. If the electrons in the state $|E_g; el\rangle \otimes |E_{ex}; phonon\rangle$ are scattered to the Γ point by absorbing optical phonons, the second step transition from the state $|E_g; el\rangle \otimes |E_{ex'}; phonon\rangle$ to the state $|E_g; el\rangle \otimes |E_{ex_{thermal}}; phonon\rangle$ becomes possible, resulting in photon emission, as in the case of a direct transition-type semiconductor. This is process (1) shown in Figure 1(b). Here, $|E_{ex}; phonon\rangle$ and $|E_{ex'}; phonon\rangle$ are the excited states that the phonon reached before and after absorbing optical phonons. The energy of the emitted photons is $h\nu_{anneal} + h\nu_p$, where $h\nu_p$ is the energy of the optical phonon.

Process (1[†]) represents the second-step transition from the intermediate state $|E_g; el\rangle \otimes |E_{ex}; phonon\rangle$ to the final state

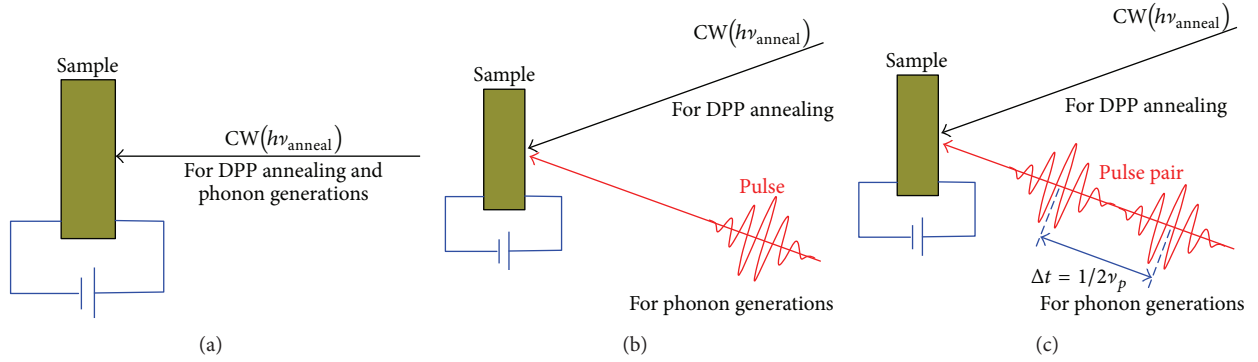


FIGURE 2: Illustration of DPP-assisted annealing using (a) CW light (conventional process); (b) CW light and a light pulse; and (c) CW light and two light pulses.

$|E_g; e\rangle \otimes |E_{\text{ex}}^{\text{thermal}}; \text{phonon}\rangle$, which occurs via emission of an optical phonon. Thus, it is conjugate to process (1). In this process, $|E_{\text{ex}}^n; \text{phonon}\rangle$ in Figure 1 shows the phonon excited state after the emission of the optical phonon. The emitted photon energy is $h\nu_{\text{anneal}} - h\nu_p$.

Similarly, processes (n) and (n^\dagger) are transitions in which n optical phonons are absorbed or emitted. Since, in practice, the processes (n) and (n^\dagger) occur simultaneously, sidebands with photon energies $h\nu_{\text{anneal}} - nh\nu_p$ and $h\nu_{\text{anneal}} + nh\nu_p$ appear in the emission spectrum. The relationship between the n th order sideband energy and the photon energy $h\nu_{\text{anneal}}$ is the same as that of an n th order Raman scattering process with respect to the zero-phonon line. As is well-known, in Raman scattering, when a large number of phonons are excited, the electrons absorb them, emitting light. On the other hand, when a small number of phonons are excited, the electrons emit phonons, emitting light [17]. Thus, the intensity of these sidebands changes according to the number of phonons. This suggests that the intensity of the sidebands can be controlled by controlling the number of phonons.

3. Principle of Controlling the Number of Phonons

The number of created phonons can be controlled by a method involving multiphoton absorption or coherent phonon (CP) excitation using pulsed light. Since the Si crystal is heated by DPP-assisted annealing in the present work, resonant absorption to a specific exciton state for creation of coherent phonons is not possible by using a high-power CW-laser optical source. This is because the high-power CW laser excitation dose not change only the phonon structures but also DP state. Therefore, we decided to selectively create phonons via CP excitation using ultrashort pulsed light. The principle of the CP excitation in this case can be understood as an impulsive stimulated Raman scattering (ISRS) process, which is a kind of stimulated Raman scattering [18]. The duration and the repetition rate of the used pulsed light were 17 fs and 80 MHz, respectively. Therefore, its duty ratio was 1.3×10^{-6} . The Raman process is based on the third order optical nonlinearity. Therefore, the enough laser power for the control of CP generation using the ultrashort pulsed light is 2.3×10^{-18} times lower than that using the CW laser.

Thus, in the experiment, the adverse effect was reduced to the negligible small coming from the DP generation by the additional laser excitation for the CP control.

In ISRS, the frequency component of the pulsed light irradiating the crystal includes coherent frequency components ν and $\nu - \nu_p$ with sufficiently high intensity, where ν_p is the phonon vibration frequency. Therefore, when the crystal is irradiated with pulsed light, the electrons absorb light with energy $h\nu$ and exhibit stimulated emission of light with energy $h\nu - h\nu_p$. At this time, it is possible to create CPs having an energy $h\nu_p$. Since these CPs are coherent, it is possible to control the creation of CPs by a single pulse or multiple pulses of light and causing them to interfere. In other words, unlike conventional DPP-assisted annealing in which the Si crystal is irradiated with CW light, CP creation is controlled by irradiating the Si crystal with pulsed light in addition to CW light. Therefore, it is possible to control the intensities of the sidebands in the EL spectrum. In the following, we describe the case where the Si-LED is irradiated with a single pulse of light during the DPP-assisted annealing and the case where the Si-LED is irradiated with a pair of light pulses.

(1) *Irradiation with a Single Light Pulse.* In the conventional DPP-assisted annealing, as shown in Figure 2(a), the CW light plays the role of decreasing the thermal diffusion rate by means of stimulated emission. In our approach, as shown in Figure 2(b), a light pulse is also radiated, together with the CW light. Since the light pulse excites multimode CPs via ISRS, the coupling probability of electron-hole pairs, photons, and CPs increases. As a result, the probability of electrons absorbing phonons and emitting light increases because the number of excited phonons increases as the light emission intensity increases. Therefore, the intensity of the sidebands having energy $h\nu_{\text{anneal}} + nh\nu_p$ increases, and the intensity of sidebands having energy $h\nu_{\text{anneal}} - nh\nu_p$ decreases. Thus, compared with an Si-LED fabricated by irradiation with only CW light, it is expected that the EL spectral shape of the Si-LED will show a higher light emission intensity at energies higher than $h\nu_{\text{anneal}}$ and conversely a lower light emission intensity at energies lower than $h\nu_{\text{anneal}}$.

(2) *Irradiation with Two Light Pulses (Light Pulse Pair).* Since the CPs created by ISRS are coherent and thus have the ability

to interfere, as described above, let us consider the case where a Si crystal is sequentially irradiated with two coherent light pulses having an arrival time difference Δt . If the value of Δt is a half-integer multiple of the vibration period, $1/\nu_p$, of the phonons ($n/2\nu_p$; $n = 1, 3, 5, \dots$), as shown in Figure 2(c), it is known that the excited CPs destructively interfere [19]. On the other hand, they constructively interfere when Δt is an integer multiple of the vibration period (n/ν_p ; $n = 1, 2, 3, \dots$). That is to say, by radiating a pair of light pulses, it is possible to control the creation of CPs so as to be suppressed or enhanced. Thus, by adjusting the value of Δt , it is possible to perform various types of sideband control as compared with (1) above.

As an example, in the case of $\Delta t = 1/2\nu_p$, we will explain how the CP creation is controlled and how, as a result of this, the EL spectrum is controlled. The value $\Delta t = 1/2\nu_p$ corresponds to one period of vibration of a phonon with frequency $2\nu_p$. Therefore, by radiating a pair of pulses having this value Δt , the number of phonons of frequency ν_p decreases, whereas the number of phonons of frequency $2\nu_p$ increases. Thus, the probability of process (1[†]) increases, by which electrons emit phonons of frequency ν_p and emit light, resulting in a higher probability of electrons absorbing phonons of frequency $2\nu_p$ and emitting light. In other words, as a result of the reduction in the number of phonons with frequency ν_p , the intensity of the sideband at energy $h\nu_{\text{anneal}} - h\nu_p$ becomes higher than that of the sideband at energy $h\nu_{\text{anneal}} + h\nu_p$. At the same time, as a result of the increase in the number of phonons with frequency $2\nu_p$, the intensity of the sideband at energy $h\nu_{\text{anneal}} - 2h\nu_p$ becomes lower than that of the sideband at energy $h\nu_{\text{anneal}} + 2h\nu_p$. The above discussion can also be extended to an explanation of the case where the sideband intensity at energy $h\nu_{\text{anneal}} - (2n - 1)\nu_p$ increases, and that at energy $h\nu_{\text{anneal}} + (2n - 1)\nu_p$ decreases. It can be also extended to the case where the sideband intensity at energy $h\nu_{\text{anneal}} - 2n\nu_p$ decreases, and that at energy $h\nu_{\text{anneal}} + 2n\nu_p$ increases. For controlling the number of phonons during the DPP-assisted annealing, we irradiate two light pulses with delay times of $\Delta t = 1/\nu_{p,\text{exp}}$ ($= 64.1$ fs), $1/2\nu_{p,\text{exp}}$ ($= 32.1$ fs), and $1/4\nu_{p,\text{exp}}$ ($= 16.0$ fs).

4. Fabrication of Si-LED and Evaluation of EL Spectrum

To fabricate a Si-LED, we doped a $625 \mu\text{m}$ -thick n -type Si (100) substrate with arsenic (As) at a concentration of about 10^{15}cm^{-3} . The resulting resistivity was $10 \Omega\text{cm}$. Next, we formed a p-n homojunction by ion implantation of boron (B) with a dose of $5 \times 10^{13} \text{cm}^{-2}$ and an acceleration energy of 700keV . Then, we deposited a transparent ITO film with a thickness of 150nm on the surface of the p layer and a Cr/Al film with a thickness of 80nm on the surface of the n layer, both by RF sputtering, to form an anode and a cathode, respectively. The device fabrication conditions up to this point were the same as those reported in [12]. In DPP-assisted annealing, we used CW laser light with energy $h\nu_{\text{anneal}} = 0.94 \text{eV}$ (wavelength $1.3 \mu\text{m}$) as the light source for creating DPs. As the pulsed light source for creating CPs,

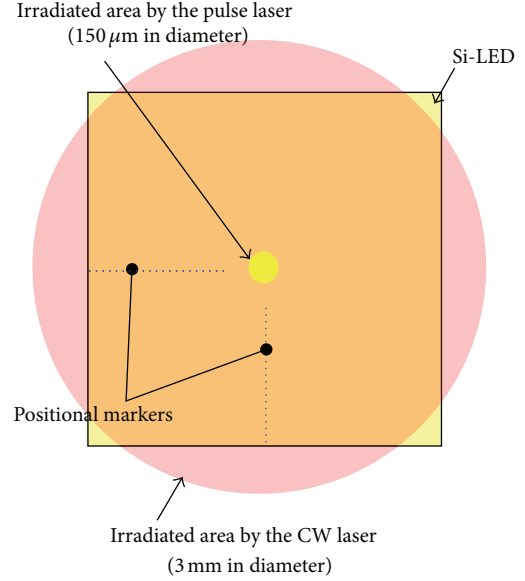


FIGURE 3: Irradiation spots of CW light and pulsed light on sample surface during DPP-assisted annealing.

we used a mode-locked laser with a photon energy of 1.55eV (wavelength $0.8 \mu\text{m}$), a pulse width of 17fs , and a repetition frequency of 80MHz . To verify the DPP-assisted annealing method, we employed the following four samples.

(a) *Sample 1.* Sample 1 was irradiated with pulsed light (average power 100mW , spot diameter $150 \mu\text{m}$) and CW light ($h\nu_{\text{anneal}} = 0.94 \text{eV}$, power 1W , spot diameter 3mm). It was annealed with a voltage of 20V and a current of 145mA for 1 hour (Figure 2(b)).

(b) *Samples 2–4.* Of the CPs created by pulsed light irradiation, we selected optical phonons with the highest creation probability [20] ($h\nu_p = 65 \text{meV}$ ($\nu_p = 15.6 \text{THz}$); indicated as $h\nu_{p,\text{exp}}$ below) as the phonons to be controlled. The samples were irradiated with CW light and a pair of light pulses with $\Delta t = 1/\nu_{p,\text{exp}}$ ($= 64.1 \text{fs}$), $1/2\nu_{p,\text{exp}}$ ($= 32.1 \text{fs}$), and $1/4\nu_{p,\text{exp}}$ ($= 16.0 \text{fs}$). They were annealed with a voltage of 25V and a current of 120mA for 1 hour (Figure 2(c)). The other experimental conditions were the same as those used for Sample 1 above. In the following, samples for $\Delta t = 1/\nu_{p,\text{exp}}$, $1/2\nu_{p,\text{exp}}$, and $1/4\nu_{p,\text{exp}}$ are referred to as Samples 2, 3, and 4, respectively.

To eliminate the contributions of variations in the sizes and shapes of the electrode and the substrate to the experimental results, the CW light was radiated onto the entire surface of the sample, and the pulsed light was radiated only at the center of the region irradiated with the CW light, as shown by the red and yellow circles, respectively, in Figure 3. With the samples prepared with this method, the EL spectral shapes in these two circles were different. By taking this difference between the intensities of these EL spectra, it was possible to eliminate the contributions above and to examine the details of the changes in the EL spectra depending on the presence/absence of the pulsed light irradiation. Experimental results are shown below.

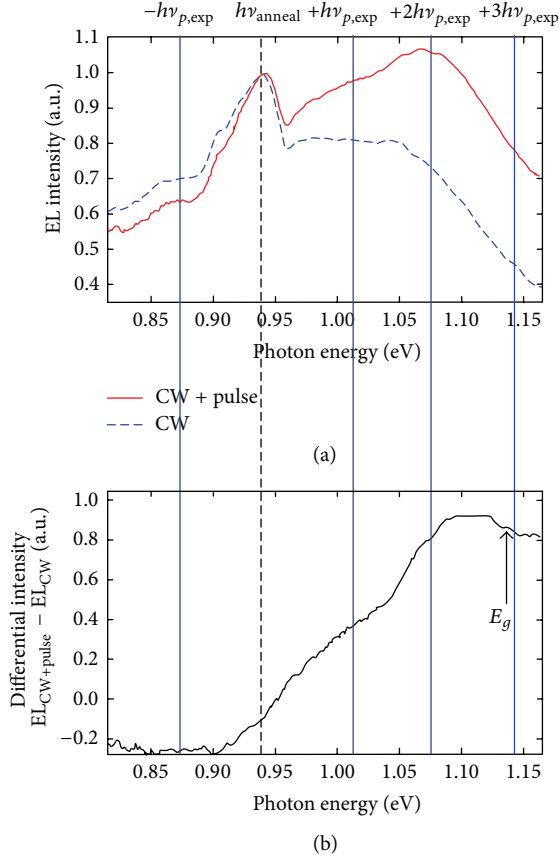


FIGURE 4: (a) EL spectra of Sample 1 after DPP-assisted annealing with the method in Figure 2(b). Red solid curve: area irradiated with CW light and pulsed light. Blue broken curve: area irradiated only with CW light. (b) Differential EL spectrum.

(a) *Sample 1.* Figure 4(a) shows, for Sample 1, the EL spectrum of the part irradiated with only the CW light (blue broken curve: EL_{CW}) and the EL spectrum of the part irradiated with the CW light and the pulsed light (red solid curve: $EL_{CW+pulse}$). Figure 4(b) shows the difference between their intensities ($EL_{CW+pulse} - EL_{CW}$; differential EL spectrum). By irradiating the sample with the pulsed light, the EL intensity at higher energies increased, and the intensity of the +1 and +2 order sidebands of the optical phonons (energy $h\nu_{p,exp} = 65$ meV) increased. In the differential EL spectrum, we also confirmed band-edge light emission and an increase in the intensity of the +3 order sideband. However, since we did not perform mode selection by using a pair of pulses, the spectra of the sidebands were extremely broad. The increase in intensity of these sidebands is explained by the creation of a large number of CPs by ISRS, using the pulsed light, as explained in Section 3. In other words, since a large number of CPs are created, the process in which CPs are absorbed becomes dominant, resulting in light emission. In addition, the increase in light emission at the band edge is considered to be a consequence of the increased number of phonons due to CP creation causing an increased probability of a direct transition between electronic bands.

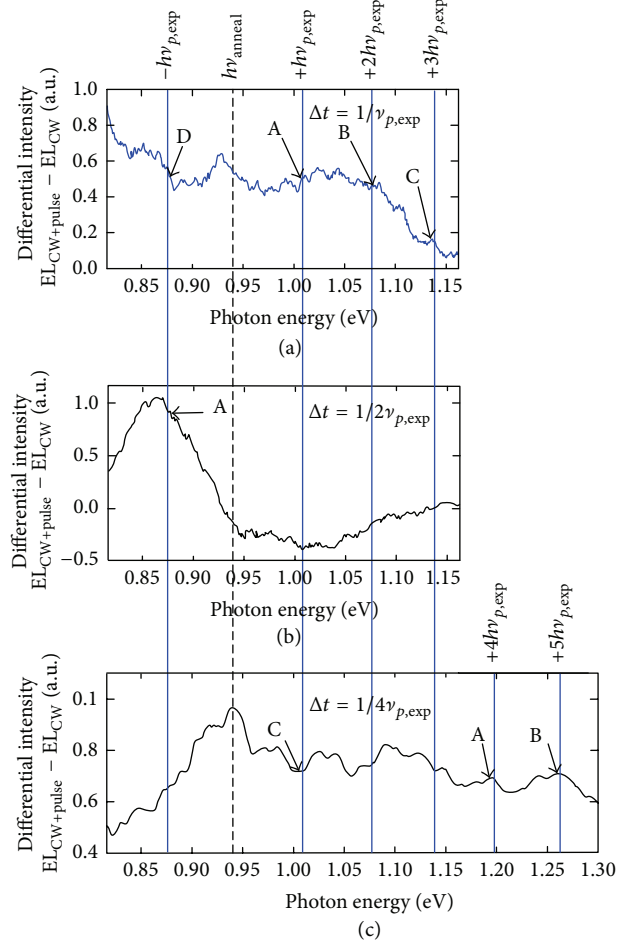


FIGURE 5: Differential EL spectra. (a) Sample 2 with $\Delta t = 1/\nu_{p,exp}$. (b) Sample 3 with $\Delta t = 1/2\nu_{p,exp}$. (c) Sample 4 with $\Delta t = 1/4\nu_{p,exp}$.

On the other hand, in the sideband corresponding to the -1 order optical phonons, the EL intensity is decreased by the incident pulsed light during DPP-assisted annealing. This is because process (1^\dagger), in which optical phonons and light are emitted, is suppressed due to CPs created by the pulsed light.

(b) *Sample 2.* Figure 5(a) shows the differential EL spectrum for Sample 2. In this sample, small bumps (arrows A, B, and C) are observed at the positions of the +1 to +3 order optical phonon sidebands ($h\nu_{p,exp} = 65$ meV). They are due to the selective creation of optical phonons $n h\nu_{p,exp}$ ($n = 1, 2, 3, \dots$), which were mode-selected by irradiating this sample with a pair of pulses with $\Delta t = 1/\nu_{p,exp}$. On the other hand, a region with reduced light emission, like that seen in Figure 4(b), was not observed in the region whose energy is lower than $h\nu_{anneal}$ (arrow D). The reason for this is that the number of created optical phonons is half or less of that in the case of Sample 1 because ISRS is a second-order nonlinear process, and the energy of the pulses irradiating this sample is one-half of the energy of the pulses irradiating Sample 1. This is due to the

suppression of process (1^\dagger), in which light emission occurs while phonons are emitted.

(c) *Sample 3.* Figure 5(b) shows the differential EL spectrum for Sample 3. In this sample, the intensity of the -1 order sideband increased (arrow A). The reason for this is that, with $\Delta t = 1/2\nu_{p,\text{exp}}$, the number of odd-numbered harmonic components was decreased, and the number of even-numbered harmonic components was increased. In other words, since the electrons had an increased probability of emitting the $+1$ order phonons, process (1^\dagger) was dominant, and the intensity of the -1 order sideband increased. On the other hand, process (1), in which light emission occurs while phonons are absorbed, is suppressed. Therefore, since the high-order modes are also suppressed, a region exhibiting reduced optical phonon sidebands is observed at energies higher than $h\nu_{\text{anneal}}$, which is the opposite to what is shown in Figure 4(b).

(d) *Sample 4.* Figure 5(c) shows the differential EL spectrum for Sample 4. The intensities of the $+1$ order and $+2$ order sidebands were decreased, and those of the $+4$ order and $+5$ order sidebands were increased. A reason for this is that, with $\Delta t = 1/4\nu_{p,\text{exp}}$, the number of $+2$ order harmonic phonons was decreased, and that the number of $+4$ order harmonic phonons was increased. The reason for the increase in the number of optical phonons in the $+5$ order is considered to be because the values of $1/4\nu_{p,\text{exp}}$ and $1/5\nu_{p,\text{exp}}$ are close. As a result, the intensity of the $+1$ order sideband is decreased. In other words, this is because the $+1$ order optical phonons are absorbed for creating the $+4$ order and $+5$ order harmonic phonons. The reason why the generation of the $+5$ order sideband dominates over generation of the $+1$ order sideband is that the energy of the $+5$ order sideband is higher than the bandgap energy, E_g , of Si, and this is a phonon scattering process that is resonant with the electronic level. As a result, process (1) is suppressed, and the intensity of the $+1$ order sideband is decreased. On the other hand, since the overall number of optical phonons is increased, process (1^\dagger) is suppressed, as in the case of Figure 4(b). As a result, a region with reduced light emission, similar to that seen in Figure 4(b), is observed in the region at energy $h\nu_{\text{anneal}} - nh\nu_{p,\text{exp}}$.

Figure 6 shows EL spectra of the regions irradiated with the light pulses for Samples 2 and 3. In Sample 2, the numbers of phonons of the fundamental ($h\nu_{p,\text{exp}}$) and the harmonics ($nh\nu_{p,\text{exp}}$; $n = 2, 3, \dots$) were all increased, and therefore, the phonon absorption probability of the electrons increased, resulting in higher light emission at higher energies. In Sample 3, on the other hand, due to the interference of CPs, the number of odd-order harmonic components of the phonons was decreased, and the number of even-order harmonic components was increased; therefore, the absorption probability of phonons of odd-order harmonic components was decreased, resulting in relatively higher light emission at lower energies. The above results indicate that the EL spectral shape of the Si-LED was successfully controlled by changing the conditions of the pair of light pulses radiated during DPP-assisted annealing. That is, the intensity at energies

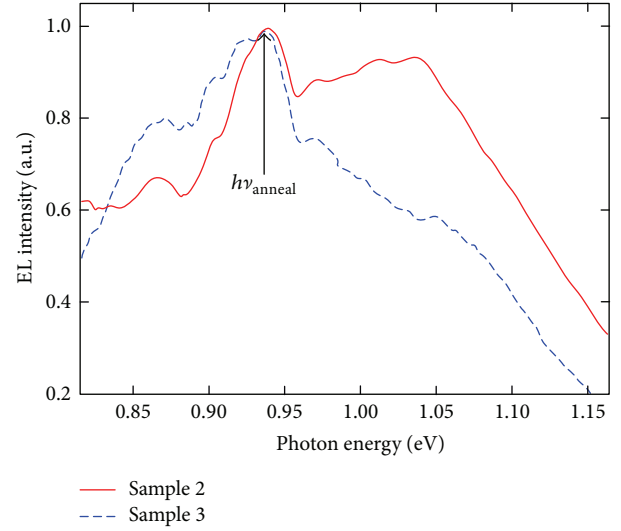


FIGURE 6: EL spectra after annealing for Samples 2 and 3.

higher than $h\nu_{\text{anneal}}$ is increased, and that at lower energies is decreased. Furthermore, conversely, the intensity at energies lower than $h\nu_{\text{anneal}}$ is increased, and that at higher energies is decreased.

In DPP-assisted annealing without using a pulsed light source, the broadening (half width at half maximum, HWHM) towards lower energies was 250 meV or greater, and the broadening (HWHM) towards higher energies was 50 meV. In contrast, in the EL spectrum of the Si-LED fabricated using a pulsed light source for creating phonons, the EL spectrum was broadened towards higher energies by 200 meV or greater (HWHM), and the broadening towards lower energies was reduced to 120 meV (HWHM).

5. Conclusion

In DPP-assisted annealing, we successfully controlled the spectral shape of a Si LED by radiating a pair of light pulses for creating CPs. In the EL spectrum, the intensity of sidebands due to phonons could be controlled by the number of phonons during DPP annealing. The peak wavelength in the EL spectrum was determined by the wavelength of the light source used in DPP-assisted annealing. In order to broaden the EL spectrum toward higher energy, a pair of light pulses having $\Delta t = 1/4\nu_{p,\text{exp}}$ was radiated. Conversely, to broaden the EL spectrum towards lower energies, a pair of light pulses having $\Delta t = 1/2\nu_{p,\text{exp}}$ was radiated. As a result, the EL spectrum was broadened towards higher energies by 200 meV or greater (HWHM), and the broadening towards lower energies was reduced to 120 meV (HWHM).

Conflict of Interests

The authors declare that there is no conflict of interests regarding the publication of this paper.

References

- [1] Z. I. Alferov, "The history and future of semiconductor heterostructures," *Semiconductors*, vol. 32, no. 1, pp. 1–14, 1998.
- [2] R. A. Milano, P. D. Dapkus, and G. E. Stillman, "An analysis of the performance of heterojunction for fiber optic communications," *IEEE Transactions on Electron Devices*, vol. 29, no. 2, pp. 266–274, 1982.
- [3] National Toxicology Program, "NTP technical report on the toxicology and carcinogenesis studies of indium phosphide (CAS No. 22398-80-7) in F344/N rats and B6C3F1 mice (inhalation studies)," Tech. Rep. NTP TR 499, U.S. Department of health and human services, Public Health Service, National Institute of Health, 2001.
- [4] K. D. Hirschman, L. Tsybeskov, S. P. Duttagupta, and P. M. Fauchet, "Silicon-based visible light-emitting devices integrated into microelectronic circuits," *Nature*, vol. 384, no. 6607, pp. 338–341, 1996.
- [5] Z. H. Lu, D. J. Lockwood, and J.-M. Baribeau, "Quantum confinement and light emission in SiO₂/Si superlattices," *Nature*, vol. 378, no. 6554, pp. 258–260, 1995.
- [6] L. Dal Negro, R. Li, J. Warga, and S. N. Basu, "Sensitized erbium emission from silicon-rich nitride/silicon superlattice structures," *Applied Physics Letters*, vol. 92, no. 18, Article ID 181105, 2008.
- [7] T. Komoda, J. Kelly, F. Cristiano et al., "Visible photoluminescence at room temperature from microcrystalline silicon precipitates in SiO₂ formed by ion implantation," *Nuclear Instruments and Methods in Physics Research B*, vol. 96, no. 1–2, pp. 387–391, 1995.
- [8] S. Yerci, R. Li, and L. Dal Negro, "Electroluminescence from Er-doped Si-rich silicon nitride light emitting diodes," *Applied Physics Letters*, vol. 97, no. 8, Article ID 081109, 2010.
- [9] S. K. Ray, S. Das, R. K. Singha, S. Manna, and A. Dhar, "Structural and optical properties of germanium nanostructures on Si(100) and embedded in high-k oxides," *Nanoscale Research Letters*, vol. 6, no. 1, article 224, 10 pages, 2011.
- [10] M. A. Green, J. Zhao, A. Wang, P. J. Reece, and M. Gal, "Efficient silicon light-emitting diodes," *Nature*, vol. 412, no. 6849, pp. 805–808, 2001.
- [11] T. Kawazoe, K. Kobayashi, S. Takubo, and M. Ohtsu, "Nonadiabatic photodissociation process using an optical near field," *Journal of Chemical Physics*, vol. 122, no. 2, Article ID 024715, 2005.
- [12] T. Kawazoe, M. A. Mueed, and M. Ohtsu, "Highly efficient and broadband Si homojunction structured near-infrared light emitting diodes based on the phonon-assisted optical near-field process," *Applied Physics B*, vol. 104, no. 4, pp. 747–754, 2011.
- [13] T. Kawazoe, M. Ohtsu, K. Akahane, and N. Yamamoto, "Si homojunction structured near-infrared laser based on a phonon-assisted process," *Applied Physics B: Lasers and Optics*, vol. 107, pp. 659–663, 2012.
- [14] H. Tanaka, T. Kawazoe, and M. Ohtsu, "Increasing Si photodetector photosensitivity in near-infrared region and manifestation of optical amplification by dressed photons," *Applied Physics B*, vol. 108, no. 1, pp. 51–56, 2012.
- [15] N. Wada, T. Kawazoe, and M. Ohtsu, "An optical and electrical relaxation oscillator using a Si homojunction structured light emitting diode," *Applied Physics B: Lasers and Optics*, vol. 108, no. 1, pp. 25–29, 2012.
- [16] M. A. Tran, T. Kawazoe, and M. Ohtsu, "Fabrication of a bulk silicon p-n homojunction-structured light-emitting diode showing visible electroluminescence at room temperature," *Applied Physics A: Materials Science and Processing*, vol. 115, no. 1, pp. 105–111, 2014.
- [17] S. K. Arora, A. J. Kothari, R. G. Patel, K. M. Chauha, and B. N. Chudasama, "Optical absorption in gel grown cadmium tartrate single crystals," *Journal of Physics*, vol. 28, no. 1, pp. 48–52, 2006.
- [18] Y.-X. Yan, E. B. Gamble Jr., and K. A. Nelson, "Impulsive stimulated scattering: general importance in femtosecond laser pulse interactions with matter, and spectroscopic applications," *The Journal of Chemical Physics*, vol. 83, no. 11, pp. 5391–5399, 1985.
- [19] M. Hase, K. Mizoguchi, H. Harima et al., "Optical control of coherent optical phonons in bismuth films," *Applied Physics Letters*, vol. 69, no. 17, pp. 2474–2476, 1996.
- [20] P. Giannozzi, S. de Gironcoli, P. Pavone, and S. Baroni, "Ab initio calculation of phonon dispersions in semiconductors," *Physical Review B*, vol. 43, no. 9, pp. 7231–7242, 1991.

Research Article

Demonstration of Controlling the Spatiotemporal Dynamics of Optical Near-Field Excitation Transfer in Y-Junction Structure Consisting of Randomly Distributed Quantum Dots

Wataru Nomura,¹ Makoto Naruse,² Masashi Aono,^{3,4} Song-Ju Kim,⁵ Tadashi Kawazoe,¹ Takashi Yatsui,¹ and Motoichi Ohtsu¹

¹ School of Engineering, The Nanophotonics Research Center, The University of Tokyo, 2-11-16 Yayoi, Bunkyo-ku, Tokyo 113-8656, Japan

² Photonic Network Research Institute, National Institute of Information and Communications Technology, 4-2-1 Nukui-kita, Koganei, Tokyo 184-8795, Japan

³ Earth-Life Science Institute, Tokyo Institute of Technology, 2-12-1 Ookayama, Meguro-ku, Tokyo 152-8550, Japan

⁴ PRESTO, Japan Science and Technology Agency, 4-1-8 Honcho, Kawaguchi-shi, Saitama 332-0012, Japan

⁵ WPI Center for Materials Nanoarchitectonics (MANA), National Institute for Materials Science, 1-1 Namiki, Tsukuba, Ibaraki 305-0044, Japan

Correspondence should be addressed to Wataru Nomura; nomura@nanophotonics.t.u-tokyo.ac.jp

Received 10 March 2014; Accepted 24 March 2014; Published 27 April 2014

Academic Editor: Chennupati Jagadish

Copyright © 2014 Wataru Nomura et al. This is an open access article distributed under the Creative Commons Attribution License, which permits unrestricted use, distribution, and reproduction in any medium, provided the original work is properly cited.

Solution searching devices that operate on the basis of controlling the spatiotemporal dynamics of excitation transfer via dressed photon interactions between quantum dots have been proposed. Long-range excitation transfer based on dressed photon interactions between randomly distributed quantum dots is considered to be effective in realizing such devices. Here, we successfully controlled the spatiotemporal dynamics of excitation transfer using a Y-junction structure consisting of randomly dispersed CdSe/ZnS core-shell quantum dots. This Y-junction structure has two “output ends” and one “tap end.” By exciting one output end with control light, we observed increased excitation transfer to the other output end via a state-filling effect. Conversely, we observed reduced excitation transfer to the output ends by irradiating the tap end with control light, due to excitation of defect levels in the tap end. These results show the possibility of controlling the optical excitation transfer dynamics between multiple quantum dots.

1. Introduction

Light excitation in quantum dots (QDs) generates dressed photons, which are light fields localized in the vicinity of the QDs, giving rise to dressed photon interactions with other nearby matter, as well as excitation energy transfer via these interactions [1]. In particular, various optical functional devices, such as logic gates called nanophotonic devices [2–4], light-harvesting devices [5], and optical signal transmitting systems [6, 7], have been realized using QDs formed of CuCl, ZnO, InAs, CdSe, and so forth, based on optical near-field excitation transfer between QDs. Nanophotonic devices have been shown to function as logic gates, such as AND, NOT, and XOR logic gates [2–4]. These devices consist of two

or three closely spaced QDs having different energy levels, and by inputting a light beam serving as a power supply and another light beam serving as a control signal, excitation energy transfer between the QDs is controlled so that the light emitted from one of the QDs serves as the output.

On the other hand, novel solution searching and decision making devices using a QD array provided with multiple output QDs have recently been proposed [8–10]. In these devices, by inputting control signals to the output QDs based on certain rules, the probability of the optical excitation being transferred uniformly to each QD is controlled to obtain a solution. In these operations, it is necessary to control the spatiotemporal dynamics of the optical excitation transfer between spatially distributed QDs. The features of these

devices are that they operate at high speed with low energy consumption since they are driven by excitation transfer based on dressed photon interactions [11]. The proposed solution searching device finds a solution to a nondeterministic polynomial (NP) time complete problem, the satisfiability problem (SAT), much faster than the WalkSAT algorithm, which is one of the fastest stochastic local search algorithms [9, 12]. The proposed decision making device exhibits high efficiency and adaptability in solving decision making problems [10].

However, although it would be ideal to utilize the models discussed in [8–10], it would be technically challenging to directly implement their architecture. One reason for this is that, in order to implement and operate this device, it is essential to fabricate a QD array in which QDs of strictly selected dimensions and number must be precisely located with nanometer-order positioning precision, as reported in [8], which is technologically demanding from the viewpoint of fabrication as the first step. In addition, another reason is the technical challenge of having to guide the control light to multiple output QDs and separately observe the output signals coming from them.

In contrast to this approach, we distributed an extremely large number of identical-size QDs randomly, and by using a structure in which an output QD is provided at the terminal end, we experimentally demonstrated the possibility of optical excitation energy transfer over distances of micrometer order via repeated dressed photon interactions between the QDs [6]. Using such a randomly distributed QD structure overcomes the fabrication difficulties mentioned above, and because of the possibility of scaling up the technique to micrometer order, it is expected that it will also be possible to overcome the technical challenges related to control and observation.

In the work reported in this paper, using a structure in which multiple QDs are randomly distributed, we experimentally investigated control of the spatiotemporal dynamics of optical excitation transfer based on dressed photon interactions between the QDs, which is a requirement for the realization of solution searching and decision making devices. Section 2 describes fundamental principles. Section 3 describes the fabricated device, experimental setup, energy transfer measurement, and characterizations. Section 4 concludes the paper.

2. Principle

First, we will explain optical excitation transfer due to dressed photon interactions and suppression of this process. As shown in Figure 1, a small QD (QD1) and a large QD (QD2) are placed in close proximity. A first excited state E11 in QD1 is resonant with a second excited state E22 in QD2 due to their size ratio of 1:1.43 [13]. When QD1 is excited by excitation light P_{in1} , a dressed photon is generated in the vicinity of QD1. The excitation energy in QD1 is transferred to E22 by dressed photon interactions and then relaxes to E21, which is the first excited state in QD2, via intersubband relaxation. Thus, the excitation energy is transferred unidirectionally (Figure 1(a)).

This is observed as emitted light P_{out2} from QD2. However, if E21, which is the level to which the excitation relaxes, has already been excited by control light P_{in2} , the excitation energy transferred to E22 cannot relax to E21, but it is transferred back to E11, and nutation occurs between E11 and E22 (Figure 1(b)). This is observed as emitted light P_{out1} from QD1, or when there is a QD in the vicinity, this leads to an increase in the probability of excitation transfer to that QD. Based on this principle, assuming that QD1, having multiple QD2's in the vicinity, is excited, by irradiating one QD2 with P_{in2} , the probability of excitation transfer to the other QD2's is changed; in other words, it is possible to control the spatiotemporal dynamics.

Next, we will explain optical excitation transfer based on dressed photon interactions in a randomly distributed QD structure. In this structure, as shown in Figure 1(c), identical-size QDs (QD1) are randomly distributed in close proximity to each other, and QD2's are placed at one location to serve as an output. The input light P_{in1} incident on the QD1's at one end undergoes repeated dressed photon interactions between the QD1's and eventually arrives at the QD2's, where it is output as emitted light P_{out2} from E21. Because the optical excitation is transferred with high probability by QDs having strong dressed photon interactions, optical excitation transfer with high energy efficiency is possible regardless of the QD1 distribution, and it has been experimentally verified that it is possible to transfer the excitation over a distance of more than 10 μm [6].

The experimental model used in this paper is shown in Figure 1(d). The green color in the figure represents a Y-junction QD1 structure consisting of a group of QD1's randomly distributed in close proximity to each other, in the form of strips with a width of 1 μm and a length of 7.5 μm extending in a radiating pattern in three directions from the center O. The ends of the Y-junction are labeled A, B, and C. QD2 structures serving as output ports, where QD2's are grouped together in squares with a side length of 3 μm , are connected at A and B so as to overlap with the QD1 structure. From A and B, called "output ends," we obtain output signals that are observed as radiation. In addition, A and B also serve as terminals for inputting control light. On the other hand, end C, which we call a "tap end," is not connected to any QD2's. The detailed experimental conditions used in this model are omitted. Figure 1(e) shows an energy band diagram in which the section including points A-O-B is illustrated one-dimensionally. When excitation light P_{in1} , serving as an input signal, is incident on the center point O in the QD1 structure, optical excitation is generated in QD1 and is transferred through the QD1 structure by undergoing repeated energy transfer due to dressed photon interactions between the QD1's. Since the optical excitation transferred to QD2 reaches E21 via intersubband relaxation, no reverse flow of the transfer occurs, and therefore the optical excitation is transferred to the ends, A and B, where the QD2 structures are provided. At this time, if end B is irradiated with control light P_{in2} that excites QD2, QD2 is excited, and the excitation light transferred from QD1 does not relax to E21, and thus excitation transfer is not observed. Therefore, a reverse flow of the optical excitation occurs at

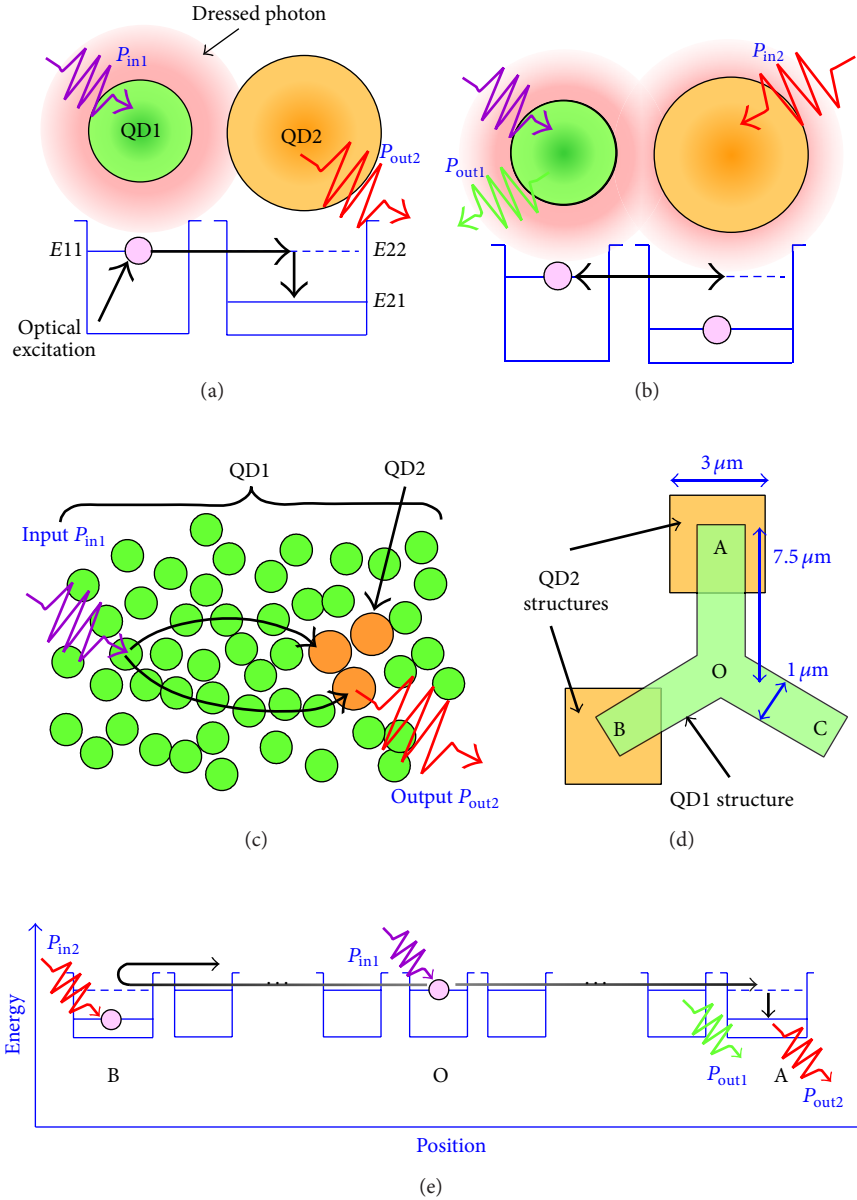


FIGURE 1: (a), (b) Schematic illustration of optical excitation transfer from QD1 to QD2 via dressed photon interactions, where (a) shows the case where energy transfer occurs from QD1 to QD2 and (b) shows the case where control light is incident on QD2, thus suppressing energy transfer. (c) Schematic diagram of long-range optical excitation transfer system. Green and yellow circles represent QD1's and QD2's, respectively. (d) Schematic diagram of experimental model. Green and yellow regions represent groups of QD1 and QD2 structures consisting of randomly distributed QD1's and QD2's, respectively. (e) Energy diagram schematically showing the experimental model from point B to point A.

end B, and the level of excitation transfer to A, which is the other output end, increases. At locations where the excitation transfer is increased, the emitted light P_{out1} and P_{out2} from QD1 and QD2 both increase, and, therefore, we can confirm that the excitation transfer is controlled by evaluating the increase in P_{out1} at end A when end B is irradiated with control light P_{in2} . Note that even if end C is irradiated with control light P_{in2} , a change like that occurring at points A and B is not expected to occur since the excitation state of the QDs does not change.

3. Experiments

3.1. Device. In our experiments, we used commercially available CdSe/ZnS core-shell QDs (manufactured by Quantum Design, Inc.). As QD1 and QD2 described in the previous section, we selected QDs with core-diameters of $d_1 = 2.5$ nm and $d_2 = 3.2$ nm, respectively. Their first excited states, estimated from absorption spectra, were $E_{11} = 2.36 \pm 0.08$ eV and $E_{21} = 2.11 \pm 0.06$ eV, respectively. As described above, E_{11} is resonant with E_{22} , which is the second excited state of QD2 [14].

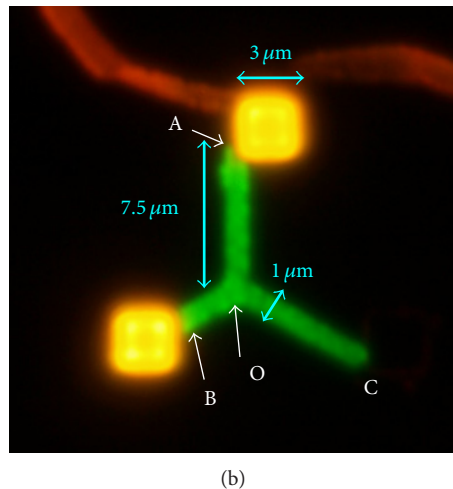
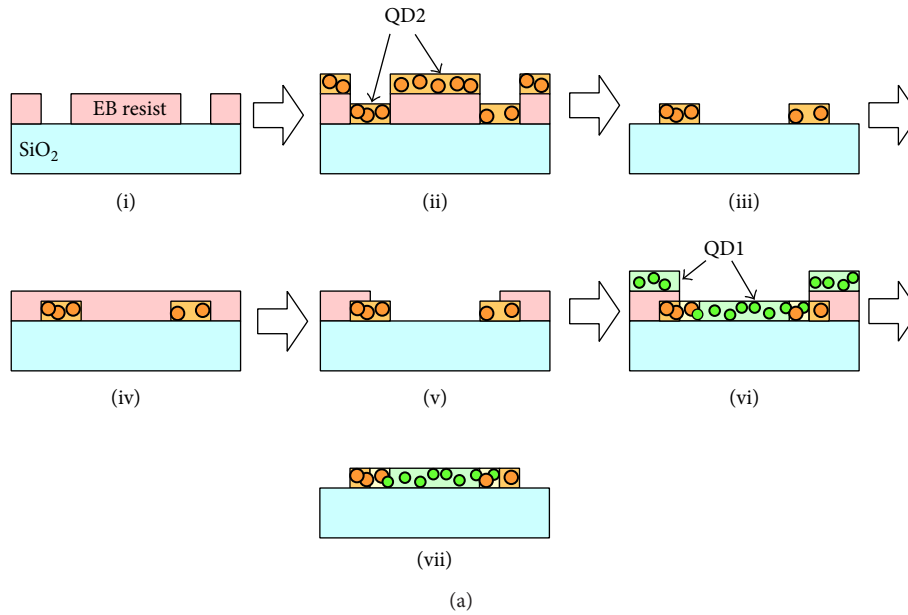


FIGURE 2: (a) Cross-sectional illustrations of sample fabrication process. (i) E-beam resist is applied to SiO₂ substrate, and regions where QD2 structures are to be formed are drawn by e-beam lithography. (ii) QD2 solution is dropped onto substrate and allowed to dry. (iii) E-beam resist is removed to obtain QD2 structures. (iv) E-beam resist is applied again. (v) Region where QD1 structure is to be formed is drawn by e-beam lithography. (vi) QD1 solution is dropped onto resist and allowed to dry. (vii) E-beam resist is removed to obtain the sample. (b) Fluorescence microscope image of sample excited by mercury vapor lamp.

The outside of the shell was modified with a carboxyl group. The solution was dropped onto a substrate and allowed to dry, affording a group of randomly distributed QDs located in close proximity with a center-to-center distance of about 10 to 20 nm.

We fabricated samples using the procedure shown in Figure 2(a). First, by using e-beam lithography on a silica substrate, in e-beam resist (ZEP-520A, Zeon Corp.), we drew locations at which QD2's were to be deposited (Figure 2(a)(i)). Next, the QD2 solution was dropped onto the substrate and allowed to dry (Figure 2(a)(ii)). Then, after removing the resist, we obtained the QD2 structure on the substrate (Figure 2(a)(iii)). Next, e-beam resist was applied on this structure (Figure 2(a)(iv)), and using e-beam lithography, we drew Y-junction locations where QD1's were

to be deposited by aligning the positions so as to contact the QD2 structure (Figure 2(a)(v)). After developing the resist, we dropped the QD1 solution onto the substrate (Figure 2(a)(vi)). Finally, the resist was removed to obtain the Y-junction QD1 structure (Figure 2(a)(vii)). Figure 2(b) shows a fluorescence microscope image obtained when the fabricated sample was excited with a mercury-vapor lamp. The QD1 structure and the QD2 structure were observed as green and yellow colors, respectively. Because points A and B were set at positions where the QD1 and QD2 structures were initially in contact, in practice the distances OA and OB of the fabricated samples were about 6.8 μm and 3.3 μm, respectively. Point C, which did not possess the QD2 structure, was set at a position 7 μm away from O.

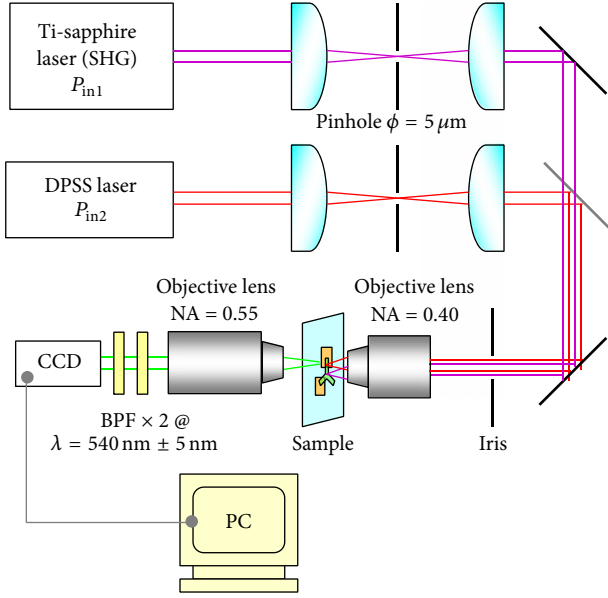


FIGURE 3: Schematic diagram of experimental setup for measurement.

3.2. Experimental Setup. The experimental setup used for performing measurements is shown in Figure 3. For the excitation light P_{in1} , we used the 2nd harmonic wave of a mode-locked Ti: sapphire laser (Mira 900, Coherent, Inc.) with a photon energy $h\nu_1 = 3.44$ eV, a pulse width of 2 ps, and a repetition frequency of 80 MHz, and for the control light P_{in2} , we used a CW diode-pumped solid state (DPSS) laser with a photon energy $h\nu_2 = 2.11$ eV. The incident powers of P_{in1} and P_{in2} were $5 \mu\text{W}$ and $10 \mu\text{W}$, respectively, and the beam spot diameters were both $5 \mu\text{m}$. The beams from the two lasers were shaped by passing them through pinholes with $5 \mu\text{m}$ diameter apertures; then, using a half-mirror, the beams irradiated the sample from the back surface of the substrate via an objective lens with a numerical aperture $\text{NA} = 0.4$. As described in the previous section, because it is possible to observe the change in excitation transfer at the output end as a variation in the emitted light P_{out1} from QD1, we evaluated this in order to make it easier to separate it from the control light. The light emitted from QD1 was observed using an electron multiplying CCD camera (Hamamatsu ImagEM C9100-13H, Hamamatsu Photonics K.K.) after passing through an objective lens with $\text{NA} = 0.55$ and two bandpass filters with transmission wavelengths of 540 ± 5 nm, which is close to the wavelength of P_{out1} . The acquired images were 512×512 pixel, 16-bit grayscale images, and the resolution was $0.37 \mu\text{m}/\text{pixel}$.

As an example of the measurement results, Figure 4(a) shows a CCD image acquired when O and A were irradiated with excitation light P_{in1} and control light P_{in2} , respectively. The green and yellow broken lines show the QD1 and QD2 structures, respectively. Point O was irradiated with P_{in1} , and we observed that the light emitted from the QD1 structure spread out in three directions due to transfer of the excitation. A cross-sectional brightness profile taken along the light-blue dotted line in this figure is shown by the red solid line in

Figure 4(b). The black solid line shows the case where point O was irradiated with only P_{in1} . The red solid line is higher in a portion of the QD1 structure serving as the transfer path OB and the point B having the QD2 structure, confirming the tendency for the optical excitation directed towards point B to be increased due to the influence of P_{in2} incident on point A.

3.3. Energy Transfer in Y-Junction Structure. To evaluate the intensity of the emitted light, we used the brightness values acquired with the CCD camera, where the total brightness of 3×3 pixels was defined as emission intensity, I . While irradiating point O with P_{in1} , we measured I_{ij} , where i indicates the output end A or B, and j indicates where the control-light P_{in2} is irradiated, that is, to the input terminal A, B, or C. Also, when no control light is irradiated, we represent this by $j = 0$. Concerning the characteristics of the device under study, described in Section 3.1, there are four representative categories:

- (a) Reference: without any P_{in2} ($j = 0$);
- (b) Case 1: emission end and control-light input terminal are the same point ($i = j$);
- (c) Case 2: emission end and control-light input terminal are opposite points ($(i, j) = (A, B)$ or (B, A));
- (d) Case 3: control-light input terminal is point C ($j = C$).

The evaluation was performed using the relative intensity change, ΔI_{ij} , defined as $\Delta I_{ij} = (I_{ij} - I_{i0})/I_{i0}$. At this time, if ΔI_{ij} is positive in Case 2, excitation transfer from one end at which the control light is input to the other end will be increased, and control of the excitation transfer will be observed.

Figure 4(c) shows a plot of ΔI_{ij} obtained in Cases 1, 2, and 3. First, we evaluated Case 1 (i.e., $i = j$), as shown by the blue bars in Figure 4(c); they took positive values $\Delta I_{AA} = 3.9 \times 10^{-2}$ and $\Delta I_{BB} = 3.7 \times 10^{-2}$, confirming that the emitted light was stronger. This is the effect of controlling the excitation transfer, and regarding energy transfer in the regions where QD1 and QD2 coexist, we obtained results showing that it is possible to control the excitation transfer also among multiple QDs. This indicates that an AND-gate operation was manifested with multiple randomly distributed QDs, as reported in [3].

Next, we evaluated Case 2 (i.e., $i \neq j = A, B$), as shown by the red bars in Figure 4(c); they also took positive values $\Delta I_{AB} = 7.3 \times 10^{-2}$ and $\Delta I_{BA} = 3.1 \times 10^{-2}$, confirming that the emitted light was stronger. ΔI_{AB} was higher than ΔI_{BA} because the wider overlapped area of QD1 and QD2 structures at point B provided more variation of excitation transfer than that at point A. This difference can be reduced by preparing finer structures and will not disturb the proper operation of solution exploring algorithms. From these results, we confirmed that the excitation transfer was suppressed by the incident control light. These results show that it is possible to control the optical excitation transfer dynamics in a randomly distributed QD structure. Since the relative change ΔI was reduced by losses involved in the optical excitation transfer, we expect that larger values will

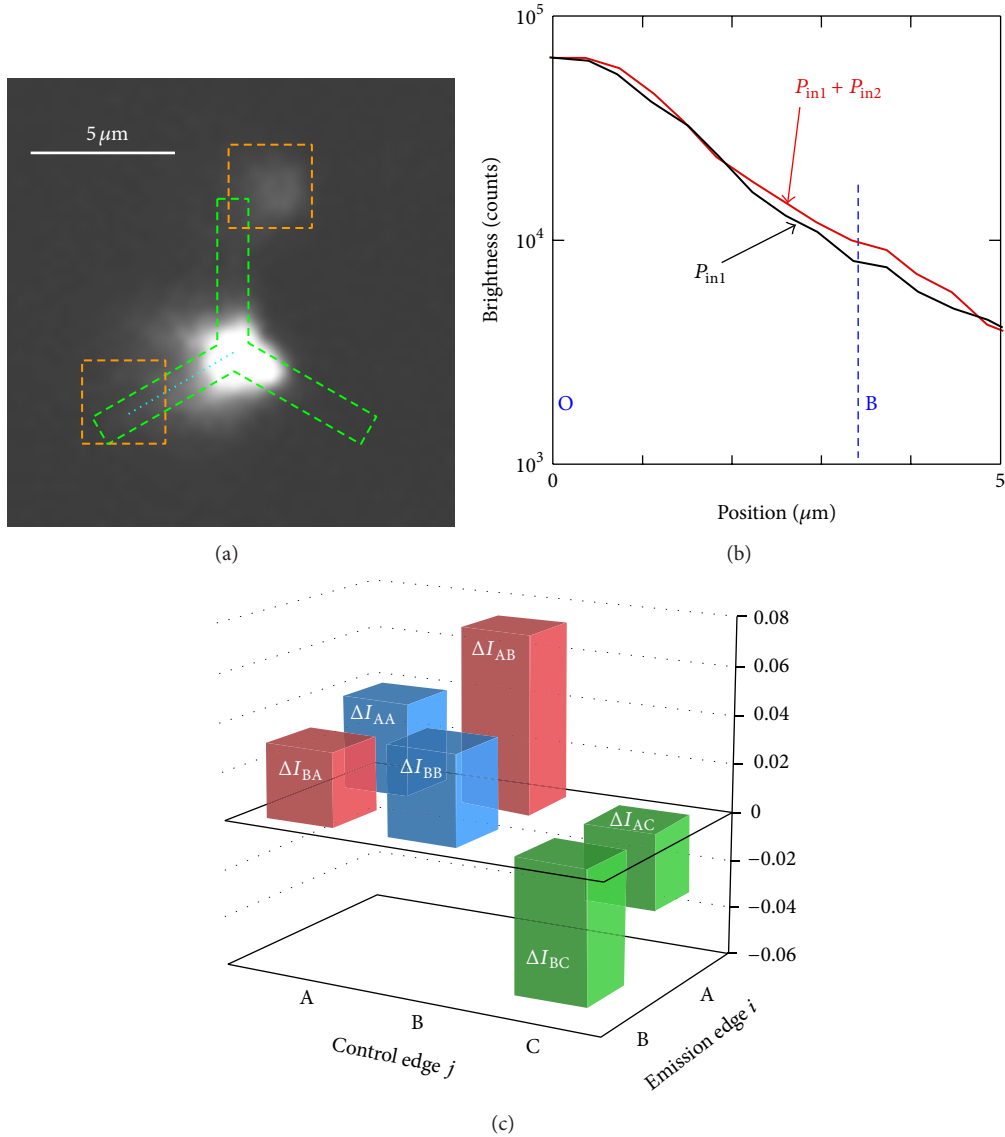


FIGURE 4: (a) Image of light emission from E11 in sample, acquired with CCD camera. Points O and A are irradiated with light P_{in1} and P_{in2} , respectively. Green and yellow broken lines represent the QD1 and QD2 structures, respectively. (b) Cross-sectional profile of emission intensity from E11, acquired with CCD. The red solid line is the cross-sectional profile taken along the light-blue dotted line in (a). The black solid line is the cross-sectional profile taken along the same location, when point O was irradiated with P_{in1} only. The $0 \mu\text{m}$ base point and the blue broken line indicate point O and point B, respectively. (c) Graph of relative change ΔI_{ij} in emission intensity from E11. Blue, red, and green bars represent Cases 1, 2, and 3, respectively.

be possible by designing a structure having shorter distances OA and OB.

3.4. Discussion on Negative Intensity Change. Moreover, we evaluated Case 3 (i.e. $j = C$), as shown by the green bars in Figure 4(c); they took negative values $\Delta I_{AC} = -3.2 \times 10^{-2}$ and $\Delta I_{BC} = -5.5 \times 10^{-2}$. Ideally, QD1 should be transparent to P_{in2} ; however, in our experiments, defect levels with energies lower than E11 in QD1 were excited by P_{in2} [15, 16]. We consider that this excitation prevented the excitation in E11 from slow and nonradiative relaxation via the defect levels.

To verify this, we performed photoluminescence measurements on the QD1 structure. In this experiment, we used samples having only the QD1 structure, fabricated with the same process as that used to fabricate the measurement samples, and we performed measurements with an experimental setup in which the bandpass filters and the CCD camera in the setup shown in Figure 3 were replaced with a spectrometer. The incident powers of P_{in1} and P_{in2} were $5 \mu\text{W}$ and $770 \mu\text{W}$, respectively, and the beams irradiated the sample in spot diameters of $10 \mu\text{m}$. The emission intensities were integrated in the range $2.25 < h\nu < 2.29 \text{ eV}$, corresponding to the peak wavelength of P_{out1} , and were normalized to the

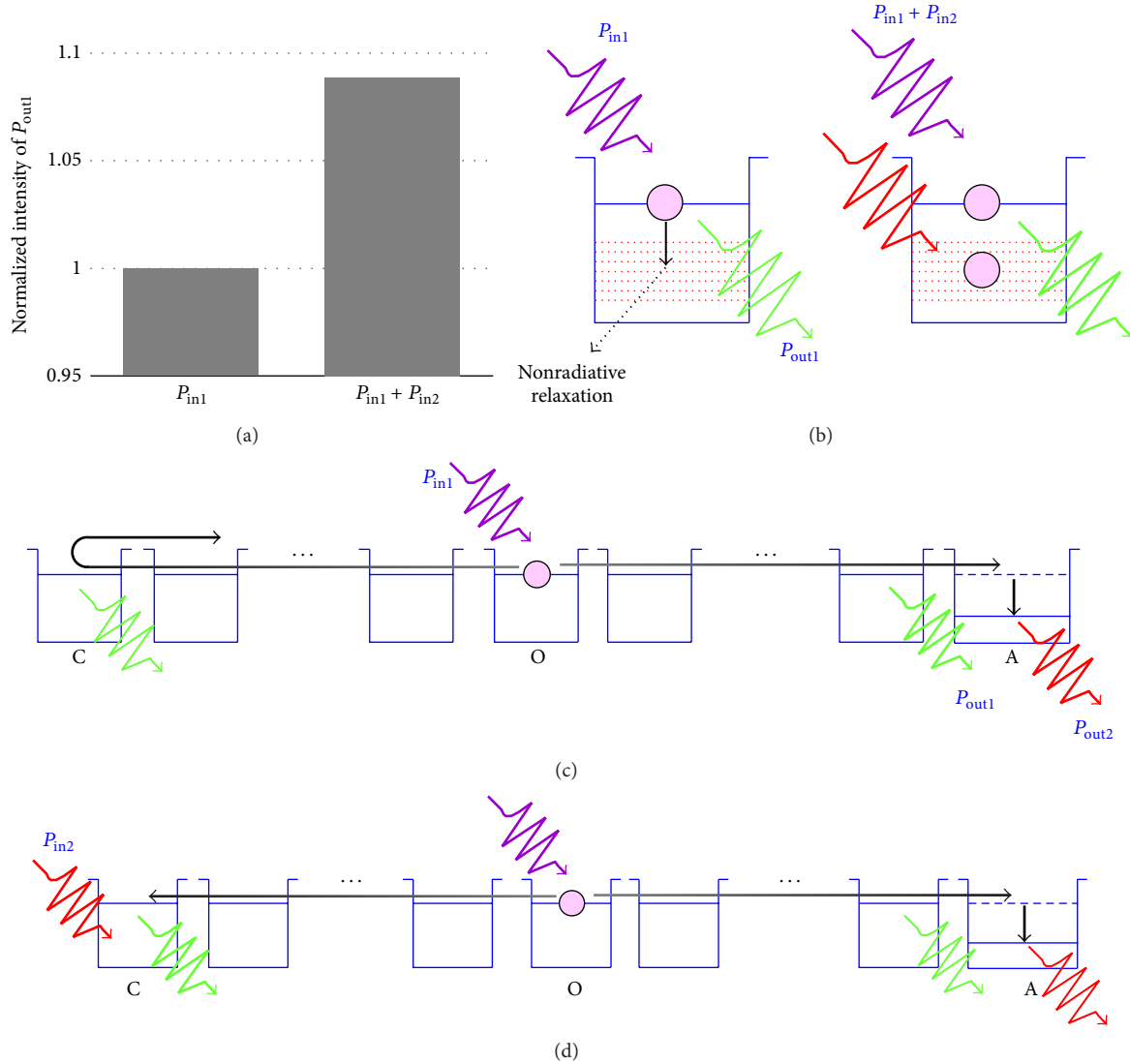


FIGURE 5: (a) Normalized intensity of emitted light P_{out1} from E11, showing cases where the QD1 structure was irradiated with only P_{in1} and with both P_{in1} and P_{in2} . (b) Schematic image of emission from QD1 with only P_{in1} or with both P_{in1} and P_{in2} . (c), (d) Energy diagram schematically showing the experimental sample from point C to point A: (c) without P_{in2} , (d) point C irradiated with P_{in2} .

emission intensity when only P_{in1} was radiated and were compared. As a result, the emission intensity for the case where P_{in1} and P_{in2} were simultaneously radiated was 1.09, showing that the emitted light was increased by radiating P_{in2} (Figure 5(a)). This was the result of defect levels in QD1 being excited by P_{in2} , suppressing the nonradiative relaxation process from E11 via defect levels, which increased the emitted light (Figure 5(b)).

From this result, the negative ΔI values in Case 3 can be explained as follows. Without P_{in2} , the excitation transferred to end C reflects and enhances P_{out1} at ends A and B (Figure 5(c)). By irradiating end C with P_{in2} , P_{out1} at C increases due to excitation of defect levels in QD1, and the reflection decreases (Figure 5(d)). As a result, P_{out1} at ends A and B decreases by irradiation of C with P_{in2} . This differs from the principle of excitation transfer suppression described

in Section 2 and Figure 1(e) but indicates the possibility of another method of controlling the spatiotemporal dynamics of excitation transfer. Also, this increased light emission due to the fact that excitation of defect levels can also occur in QD1 at points A and B; however, the energy transfer suppression effect due to excitation of E21 should be larger than this because absorption of P_{in2} ($h\nu_2 = 2.11$ eV) in QD2 is 24 times higher than that in QD1. Thus, the effect of excitation of defect levels at ends A and B is negligible.

4. Summary

In summary, to show the possibility of controlling the spatiotemporal dynamics of optical excitation transfer based on dressed photon interactions between multiple randomly distributed quantum dots (QDs), we conducted experiments

to control excitation transfer using randomly distributed QD structures. Using CdSe/ZnS core-shell QDs, we fabricated a Y-junction structure composed of randomly distributed QDs (QD1 structure). Optical excitation incident at the center of this structure was transferred to a QD2 structure serving as an output end located 3–7 μm away, and by irradiating a QD2 structure at another end with control light $P_{\text{in}2}$, we observed a maximum increase of 7.3×10^{-2} . Thus, we have shown, for the first time, that it is possible to control the spatiotemporal dynamics of optical excitation transfer in a randomly distributed QD structure. Our findings will lead to simplified implementation and driving of solution searching and decision making devices based on the optical excitation transfer dynamics between QDs and will contribute to their practical realization. On the other hand, when control light $P_{\text{in}2}$ was incident on the output end that did not have a QD2 structure, we found that the amount of excitation energy transferred to the output end was reduced by a maximum of 5.5×10^{-2} . This was thought to be because the light emission from QD1 was increased due to excitation of defect levels in QD1, and the amount of excitation energy transferred to the end provided with the QD2 structure serving as an output was reduced. This effect acted in a direction causing a reduction in excitation transfer, opposite to the increased transfer level due to excitation of the QD2 structure, indicating the possibility of a different kind of control of the spatiotemporal dynamics. This result is expected to lead to the development of novel computing device architectures in the future.

Conflict of Interests

The authors declare that there is no conflict of interests regarding the publication of this paper.

Acknowledgment

A part of this work was supported by the “Development of Next-generation High-performance Technology for Photovoltaic Power Generation System” Program, NEDO, Japan.

References

- [1] M. Ohtsu, T. Kawazoe, T. Yatsui, and M. Naruse, “Nanophotonics: application of dressed photons to novel photonic devices and systems,” *IEEE Journal on Selected Topics in Quantum Electronics*, vol. 14, no. 6, pp. 1404–1417, 2008.
- [2] T. Kawazoe, K. Kobayashi, S. Sangu, and M. Ohtsu, “Demonstration of a nanophotonic switching operation by optical near-field energy transfer,” *Applied Physics Letters*, vol. 82, no. 18, pp. 2957–2959, 2003.
- [3] T. Kawazoe, M. Ohtsu, S. Aso et al., “Two-dimensional array of room-temperature nanophotonic logic gates using InAs quantum dots in mesa structures,” *Applied Physics B: Lasers and Optics*, vol. 103, no. 3, pp. 537–546, 2011.
- [4] A. Karimkhani and M. K. Moravvej-Farshi, “Design of three-input nanophotonic and gates,” *Journal of the Optical Society of America B: Optical Physics*, vol. 26, no. 5, pp. 1084–1090, 2009.
- [5] T. Kawazoe, K. Kobayashi, and M. Ohtsu, “Optical nanofountain: a biomimetic device that concentrates optical energy in a nanometric region,” *Applied Physics Letters*, vol. 86, no. 10, Article ID 103102, pp. 1–3, 2005.
- [6] W. Nomura, T. Yatsui, T. Kawazoe, M. Naruse, and M. Ohtsu, “Structural dependency of optical excitation transfer via optical near-field interactions between semiconductor quantum dots,” *Applied Physics B: Lasers and Optics*, vol. 100, pp. 181–187, 2010.
- [7] P. Holmström, L. Thylén, and A. Bratkovsky, “Composite metal/quantum-dot nanoparticle-array waveguides with compensated loss,” *Applied Physics Letters*, vol. 97, Article ID 073110, 2010.
- [8] M. Naruse, M. Aono, S.-J. Kim et al., “Spatiotemporal dynamics in optical energy transfer on the nanoscale and its application to constraint satisfaction problems,” *Physical Review B*, vol. 86, Article ID 125407, 2012.
- [9] M. Aono, M. Naruse, S.-J. Kim et al., “Amoeba-inspired nanoarchitectonic computing: solving intractable computational problems using nanoscale photoexcitation transfer dynamics,” *Langmuir*, vol. 29, no. 254, pp. 7557–7564, 2013.
- [10] S.-J. Kim, M. Naruse, M. Aono, M. Ohtsu, and M. Hara, “Decision maker based on nanoscale photo-excitation transfer,” *Scientific Reports*, vol. 3, Article ID 2370, 2013.
- [11] M. Naruse, H. Hori, K. Kobayashi, P. Holmström, L. Thylén, and M. Ohtsu, “Lower bound of energy dissipation in optical excitation transfer via optical near-field interactions,” *Optics Express*, vol. 18, no. 23, pp. A544–A553, 2010.
- [12] U. Schöning, “A probabilistic algorithm for k-SAT and constraint satisfaction problems,” in *Proceedings of the 40th IEEE Symposium on Foundations of Computer Science*, pp. 410–414, 1999.
- [13] N. Sakakura and Y. Masumoto, “Persistent spectral-hole-burning spectroscopy of CuCl quantum cubes,” *Physical Review B—Condensed Matter and Materials Physics*, vol. 56, no. 7, pp. 4051–4055, 1997.
- [14] C. Trallero-Giner, A. Debernardi, M. Cardona, E. Menéndez-Proupín, and A. I. Ekimov, “Optical vibrons in CdSe dots and dispersion relation of the bulk material,” *Physical Review B—Condensed Matter and Materials Physics*, vol. 57, no. 8, pp. 4664–4669, 1998.
- [15] M. Y. Valakh, Y. G. Sadfyev, N. O. Korsunskaya et al., “Deep-level defects in CdSe/ZnSe QDs and giant anti-stokes photoluminescence,” *Semiconductor Physics, Quantum Electronics and Optoelectronics*, vol. 5, no. 3, pp. 254–257, 2002.
- [16] M. Danek, K. F. Jensen, C. B. Murray, and M. G. Bawendi, “Synthesis of luminescent thin-film CdSe/ZnSe quantum dot composites using CdSe quantum dots passivated with an overlayer of ZnSe,” *Chemistry of Materials*, vol. 8, no. 1, pp. 173–180, 1996.